

# Gaia Early Data Release 3 – Catalogue validation

C. Fabricius<sup>1,\*</sup>, X. Luri<sup>1</sup>, F. Arenou<sup>2</sup>, C. Babusiaux<sup>3,2</sup>, A. Helmi<sup>4</sup>, T. Muraveva<sup>5</sup>, C. Reylé<sup>6</sup>, F. Spoto<sup>7</sup>, A. Vallenari<sup>8</sup>, T. Antoja<sup>1</sup>, E. Balbinot<sup>4</sup>, C. Barache<sup>9</sup>, N. Bauchet<sup>2</sup>, A. Bragaglia<sup>5</sup>, D. Busonero<sup>10</sup>, T. Cantat-Gaudin<sup>1</sup>, J. M. Carrasco<sup>1</sup>, S. Diakité<sup>6</sup>, M. Fabrizio<sup>11,12</sup>, F. Figueras<sup>1</sup>, A. Garcia-Gutierrez<sup>1</sup>, A. Garofalo<sup>5</sup>, C. Jordi<sup>1</sup>, P. Kervella<sup>13</sup>, S. Khanna<sup>4</sup>, N. Leclerc<sup>2</sup>, E. Licata<sup>10</sup>, S. Lambert<sup>9</sup>, P. M. Marrese<sup>11,12</sup>, A. Masip<sup>1</sup>, P. Ramos<sup>1</sup>, N. Robichon<sup>2</sup>, A. C. Robin<sup>6</sup>, M. Romero-Gómez<sup>1</sup>, S. Rubele<sup>8</sup>, M. Weiler<sup>1</sup>

- <sup>1</sup> Dept. FQA, Institut de Ciències del Cosmos, Universitat de Barcelona (IEEC-UB), Martí i Franquès 1, E-08028 Barcelona, Spain  
<sup>2</sup> GEPI, Observatoire de Paris, Université PSL, CNRS, 5 Place Jules Janssen, 92190 Meudon, France  
<sup>3</sup> Univ. Grenoble Alpes, CNRS, IPAG, 38000 Grenoble, France  
<sup>4</sup> Kapteyn Astronomical Institute, University of Groningen, Landleven 12, 9747 AD Groningen, The Netherlands  
<sup>5</sup> INAF - Osservatorio di Astrofisica e Scienza dello Spazio di Bologna, via Piero Gobetti 93/3, 40129 Bologna, Italy  
<sup>6</sup> Institut UTINAM, CNRS, OSU THETA Franche-Comté Bourgogne, Univ. Bourgogne Franche-Comté, 25000 Besançon, France  
<sup>7</sup> Harvard-Smithsonian Center for Astrophysics, 60 Garden St., MS 15, Cambridge, MA 02138, USA  
<sup>8</sup> INAF, Osservatorio Astronomico di Padova, Vicolo Osservatorio, Padova, I-35131, Italy  
<sup>9</sup> SYRTE, Observatoire de Paris, Université PSL, CNRS, Sorbonne Université, LNE, 61 avenue de l'Observatoire, 75014 Paris, France  
<sup>10</sup> INAF - Osservatorio Astrofisico di Torino, Via Osservatorio 20, 10025 Pino Torinese, Torino, Italy  
<sup>11</sup> INAF - Osservatorio Astronomico di Roma, Via di Frascati 33, 00078 Monte Porzio Catone (Roma), Italy  
<sup>12</sup> ASI Science Data Center, Via del Politecnico, Roma  
<sup>13</sup> LESIA, Observatoire de Paris, Université PSL, CNRS, Sorbonne Université, Université de Paris, 5 place Jules Janssen, 92195 Meudon, France

## ABSTRACT

**Context.** The third *Gaia* data release is published in two stages. The early part, *Gaia* EDR3, gives very precise astrometric and photometric properties for nearly two billion sources together with seven million radial velocities from *Gaia* DR2. The full release, *Gaia* DR3, will add radial velocities, spectra, light curves, and astrophysical parameters for a large subset of the sources, as well as orbits for solar system objects.

**Aims.** Before the publication of the catalogue, many different data items have undergone dedicated validation processes. The goal of this paper is to describe the validation results in terms of completeness, accuracy, and precision for the *Gaia* EDR3 data and to provide recommendations for the use of the catalogue data.

**Methods.** The validation processes include a systematic analysis of the catalogue contents to detect anomalies, either individual errors or statistical properties, using statistical analysis and comparisons to the previous release as well as to external data and to models.

**Results.** *Gaia* EDR3 represents a major step forward, compared to *Gaia* DR2, in terms of precision, accuracy, and completeness for both astrometry and photometry. We provide recommendations for dealing with issues related to the parallax zero point, negative parallaxes, photometry for faint sources, and the quality indicators.

**Key words.** catalogs – astrometry – techniques: photometric

## 1. Introduction

The third data release from the European Space Agency mission *Gaia* (Gaia Collaboration et al. 2016, 2020) covers observations made between July 2014 and May 2017. It takes place in two stages, where the first (early) stage, *Gaia* EDR3, provides the updated astrometry and photometry. For convenience it also includes (nearly all) radial velocities from the second data release, *Gaia* DR2 (Gaia Collaboration et al. 2018). The second stage, the full *Gaia* DR3, will include the same sources as *Gaia* EDR3 and add new radial velocities, spectra, light curves, astrophysical parameters, and orbits for solar system objects, as well as a detailed analysis of quasars and extended objects, for example.

This paper describes the validation of *Gaia* EDR3 with the aim of facilitating the optimal use of the catalogue, comprehending its contents, and especially exposing the known issues. The approach followed is a transverse analysis of the properties of the various contents from an internal as well as external point of view. We also use the previous release, *Gaia* DR2, as a reference for comparisons in order to quantify the changes and improvements from one release to the next.

The general properties of the catalogue are described in Sect. 2. This includes the completeness in terms of limiting magnitude and angular resolution and also in terms of high proper motion stars. Likewise, we discuss how sources, and their identifiers, have changed since *Gaia* DR2.

The new astrometric solution (Lindegren et al. 2020b; Klioner et al. 2020) determines two parameters (position), ‘2p’, five parameters (position, parallax, proper motion), ‘5p’, or six

\* Corresponding author: C. Fabricius  
e-mail: c.laus@fqa.ub.edu

parameters, ‘6p’, for a source. In the latter case, the sixth parameter is the source colour (effective wavelength), listed in the *Gaia* archive as the pseudocolour. The use of three levels of solutions introduces tricky issues in the validation. Another important topic is the presence of spurious solutions and the means available to identify them. The validation of the astrometry is discussed below in Sect. 3.

Cycle 3 photometry is described by Riello et al. (2020) both in terms of the various calibration steps and in terms of data quality. Important changes have been made to the background modelling, leading to improvements for  $G_{BP}$  and  $G_{RP}$  photometry, which, however, suffers from other issues in the faint end. Changes to the overall response modelling have had undesired effects in a few cases, leading to the elimination of photometry for 5.4 million sources over a wide range of brightness. The validation of the photometry is discussed in Sect. 4.

Finally, Sect. 5 presents a statistical approach to comparing *Gaia* EDR3 and *Gaia* DR2. Additionally, we describe the overall results and recommendations in Sect. 6.

Updated radial velocities will only appear in *Gaia* DR3 and, as mentioned, *Gaia* EDR3 therefore contains values copied from *Gaia* DR2. The process for the identification of sources and the validation of the velocities is described in detail in Seabroke et al. (2020) and is therefore not discussed here. As a result of this process, 14 800 radial velocities (0.2%) were discarded.

In addition to the papers mentioned above, the *Gaia* archive provides online documentation<sup>1</sup> with additional details about the data processing and the description of the data items in the published catalogue and its various accompanying tables. *Gaia* jargon is difficult to avoid and we therefore include a short dictionary of *Gaia* and *Gaia* EDR3 related terms in Appendix B.

## 2. General tests and completeness

Our general tests cover a wide range of issues from simple, yet indispensable, checks that the catalogue has been correctly populated to more sophisticated statistical tests on completeness.

### 2.1. *Gaia* DR2 sources in *Gaia* EDR3

An important question is how to find *Gaia* DR2 sources in *Gaia* EDR3 and determine whether they are still present and if they maintain their source identifiers. In general this is the case, but there are also many exceptions. In *Gaia* EDR3, we still have 96.2% of the *Gaia* DR2 sources at the same position to within 10 mas when taking *Gaia* EDR3 proper motions into account. If we, in addition, require the same identifier, we are down to 93.6%, so close to three percent of the sources now have a different identifier. This typically happens when two processes are in conflict. On-board, the transit of a single star may trigger more than one detection or a close pair may not be resolved. Later, on ground, the cross match algorithm has to decide if it is dealing with one or two sources. Since the previous data release, more information has become available and algorithms have been adapted to better handle the difficult cases. Figure 1, which is based on a representative subset, shows that sources in the range of  $10 < G < 11.5$  mag are strongly affected by this identifier change. This is a magnitude range where the on-board detection often detects two sources, rather than just one, especially in the upper rows of the focal plane, where images tend to be wider, cf. Rowell et al. (2020, fig. 11). Measures are being

<sup>1</sup> <https://gea.esac.esa.int/archive/documentation/GEDR3/index.html>

taken in the on-ground processing to essentially eliminate this issue in future data releases. Also for the brightest sources, the swarm of spurious detections they trigger on-board *Gaia* creates problems for the cross match process, and a large fraction therefore have new identifiers. These points are discussed in detail in Torra et al. (2020).

More remarkable than a change of identifier is perhaps that many *Gaia* DR2 sources have no close counterpart in *Gaia* EDR3. If we use a closeness limit of 10 mas, as many as 3.8% sources have vanished. This limit may be a little too strict, for example, for faint sources, and if we relax it to 50 mas it is only 0.61% of the sources. Going all the way to  $2''$ , 0.18% are still missing. As shown in Fig. 1, where a 50 mas limit is used, 1–2% of the brightest sources have changed. In the faint end, the fraction of missing sources is very small at 18 mag, but it increases slowly until 20.7 mag after which it rises sharply, reaching 20% at 21.1 mag. There can be many reasons for these changes, but binaries, crowding, and spurious sources are among the likely explanations.

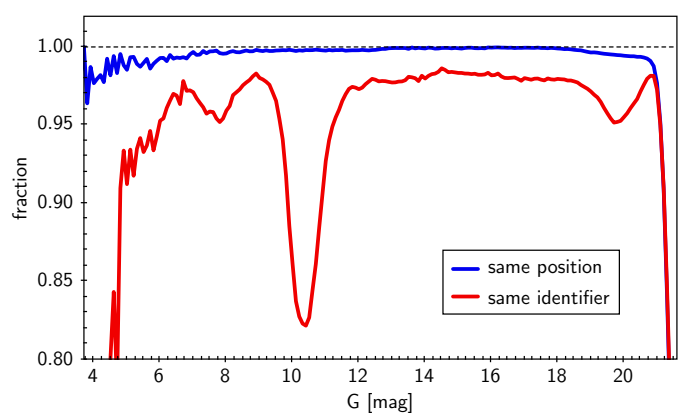


**Fig. 1.** Fraction of *Gaia* DR2 sources maintaining the same source identifier in *Gaia* EDR3 (red curve), and the fraction – irrespective of the identifier – having a counterpart in *Gaia* EDR3 at the same position within 50 mas (blue curve).

On the other hand, counterparts may be offset for good reasons. For double stars we may, for example, have only the photocentre in *Gaia* DR2, but a resolved pair in *Gaia* EDR3. It can also be that the proper motion is unknown or erroneous, and this can be important even when propagating positions by the mere 0.5 yr, which is the difference in epoch between the two catalogues. Counterparts may also be completely missing, for example, if the detections upon which the *Gaia* DR2 source was based are now considered spurious.

A table, `gaiaedr3.dr2_neighbourhood`, is provided in the *Gaia* archive. We recommend using this table for looking up *Gaia* DR2 sources in *Gaia* EDR3.

### 2.2. Large-scale completeness of *Gaia* EDR3

On-board *Gaia*, sources are selected for observation based on two criteria: they must be roughly pointlike and they must be brighter than  $G = 20.7$  mag. The instrument has, however, a limited capacity for the number of simultaneous observations, cf. de Bruijne et al. (2015), and when scanning close to the Galactic plane some observations – in particular the fainter – are never sent to ground because of limited mass-memory and telemetry capacity. As a simple measure of the actual magnitude limit, Fig. 2 shows the 99th percentile of the  $G$  magnitude across

the sky using the healpix spatial index (Górski et al. 2005). The area with the brightest limit is Baade’s window, unsurprisingly, followed by low Galactic latitudes in general. Here, the finite on-board resources clearly dominate. The limit is fainter on higher latitudes, especially along the caustics of the scanning law, where more transits are available.

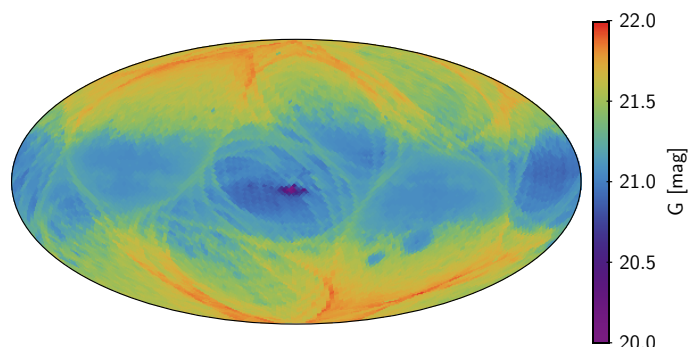


**Fig. 2.** Map in Galactic coordinates of the 99th percentile of the  $G$  magnitude at healpix level 5, i.e. in  $3.36 \square^\circ$  pixels.

Another way to estimate the completeness is to look at how the actual number of transits obtained for each source depends on the magnitude as illustrated in Fig. 3. It shows the first, third, and fifth percentiles of the number of transits and the number of visibility periods<sup>2</sup> used in the astrometric solution. For a magnitude range where the catalogue is nearly complete, we expect these percentiles for the number of transits to lie well above the required minimum of five transits for a source. For the catalogue in general (top panel), this holds for sources brighter than  $G \sim 19$  mag; however, when we reach  $G \sim 20$  mag, the incompleteness is noticeable. For a field in Baade’s window (lower panel), sources are deprived of transits at a much earlier point and the incompleteness is severe at  $G \sim 19$  mag.

The number of visibility periods used for astrometry is also of interest because a minimum of nine periods is required in order to publish the parallax and proper motion, cf. Lindegren et al. (2020b). Here, an insufficient number of periods is noticeable in the catalogue beyond  $G \sim 18.5$  mag and even more severe after  $G \sim 19.5$  mag; whereas for Baade’s window, insufficiency sets in about 1.5 mag earlier. Thinking ahead to *Gaia* DR4, the mission segment covered will be twice as long as for *Gaia* EDR3, the number of transits and visibility periods will be double, and a significant improvement in completeness can be expected.

Comparisons with models have been performed to check the data for the star density as a function of the position on the sky and of  $G$  magnitude. The reference model is GOG20. It is described in detail in the online documentation<sup>3</sup> and is also released with the *Gaia* EDR3 set of catalogues.<sup>4</sup> In order to have good statistics in each pixel of the sky maps, the comparisons are done using healpix of order 4, corresponding to 3072 pixels per sky map (Fig. 4). The comparison with the GOG20 simulation shows that the overall picture of the sky densities are very well

<sup>2</sup> A visibility period, included in the *Gaia* archive as `visibility_periods_used` is the time range when a source is observed without a time gap of more than four days. From one period to the next, the scan direction has changed and a couple of months may have passed.

<sup>3</sup> [https://gea.esac.esa.int/archive/documentation/GEDR3/Data\\_processing/chap\\_simulated/](https://gea.esac.esa.int/archive/documentation/GEDR3/Data_processing/chap_simulated/)

<sup>4</sup> GOG20 is published in the *Gaia* archive in the table `gaiaedr3.gaia_source_simulation`

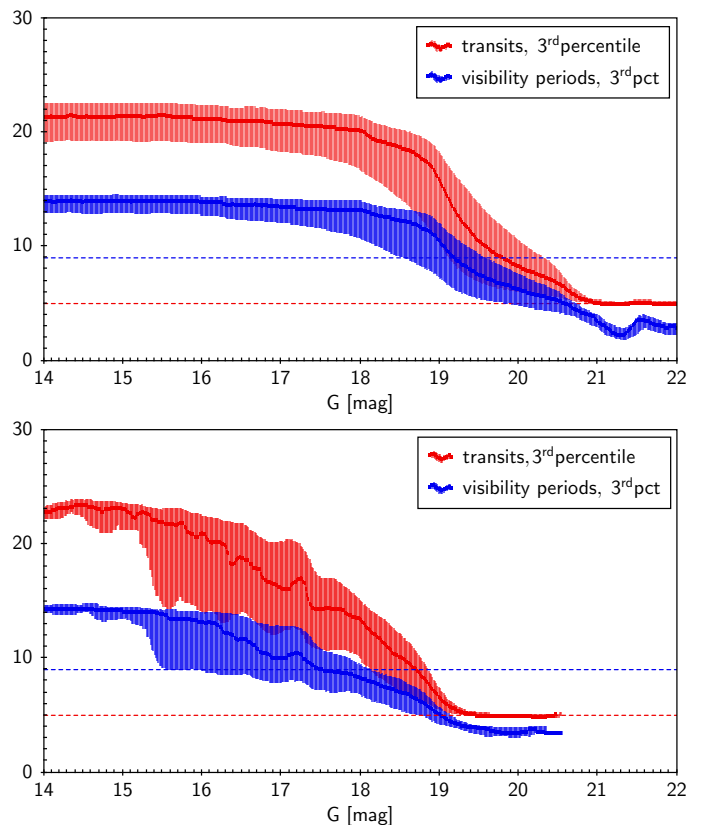


**Fig. 3.** Third percentile of the number of transits and number of visibility periods per source used in the astrometric solution. The shaded areas show the range of the first and fifth percentiles. The limits of five transits for inclusion in the catalogue and nine visibility periods for a full astrometric solution are also indicated. *Top:* The catalogue in general. *Bottom:* A field in Baade’s window.

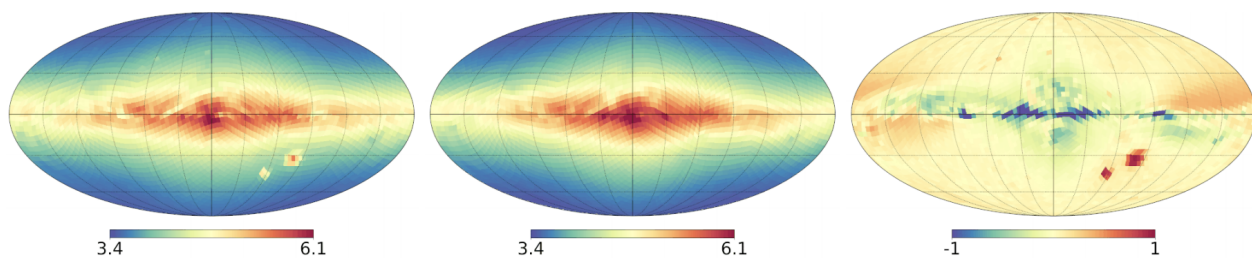
comparable in data and model, although incompleteness may remain towards the inner Galaxy for faint stars. The *Gaia* EDR3 completeness has also improved with respect to *Gaia* DR2 for stars fainter than 18 mag (Fig. 5, upper panel). Still the predicted numbers are higher than the observed, but this is mainly due to the counts in the Galactic plane, where the extinction is underestimated in GOG20 (Fig. 4, right panel, and Fig. 5, lower panel).

Figure 6 shows the improvement in the completeness of crowded regions between *Gaia* DR2 and *Gaia* EDR3. Here, we use the OGLE data from Udalski et al. (2008) which provides only an upper limit to the *Gaia* completeness due to the poorer OGLE spatial resolution.

For bright sources, detection efficiency starts to drop at  $G \sim 3$  mag due to saturation that is too strong (Gaia Collaboration et al. 2016). As a consequence, 20% of the stars brighter than magnitude 3 do not have an entry in *Gaia* EDR3. A few bright stars which were present in *Gaia* DR2 with rather dubious solutions, such as Polaris, are also missing in *Gaia* EDR3.

### 2.3. Small-scale completeness of *Gaia* EDR3

The completeness at the smallest angular separations can be tested using a histogram of source-pair distances in a small dense field near the Galactic plane. Such a field will be completely dominated by distant field stars and there will be very few resolved binaries. Figure 7 shows (top panel) a histogram of source separations for such a field, where the black line indicates the expected relation for a random source distribution. For separations



**Fig. 4.** Star counts in *Gaia* EDR3 (left), GOG20 (middle), and relative difference (right) in the magnitude range of  $17 < G < 18$ . A relative difference,  $(\text{EDR3-GOG20})/\text{EDR3}$ , of  $-1$  (resp.  $+1$ ) corresponds to an excess (resp. a deficit) of 100% in the GOG20 model with regard to *Gaia* EDR3 data. The colour scale is logarithmic in the left and middle panels, and linear in the right panel. The healpix level is 4.

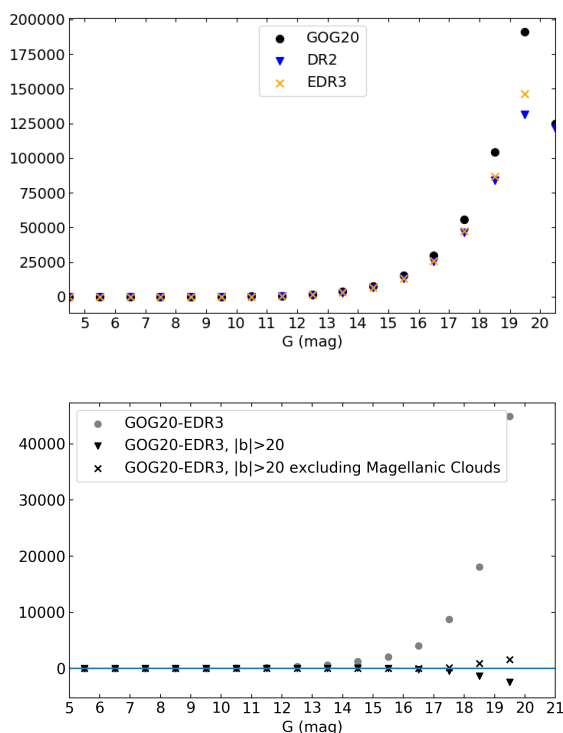


**Fig. 5.** Star counts averaged among the healpix bins over the whole sky as a function of magnitude, in *Gaia* EDR3 (orange crosses) and *Gaia* DR2 (blue triangles), compared to GOG20 (black circles). *Bottom:* Difference in counts between GOG20 and *Gaia* EDR3 over the whole sky (circles), excluding the Galactic plane (triangles), and excluding the Galactic plane and the Magellanic Clouds (crosses). The deficit in GOG20 at faint magnitudes is mainly due to the Magellanic Clouds as they are not included in the model.

above  $1.5\text{--}2''$ , the actual distribution closely follows this line, indicating that we have a high completeness. However, below  $1''.5$ , and especially below  $0''.7$ , the completeness falls rapidly. This is expected, taking the current processing strategy into account, and it is caused by conflicts between neighbour observations both wanting to use the same pixels. Between  $0''.18$  and  $0''.4$ , only a few pairs were resolved because of the particulars of their magnitude difference and their orientation with respect to the dominating scan directions. The bottom panel of the figure shows the same distribution but normalised with respect to the expected relation. This shows an apparently higher completeness for the lowest separations and the question that is begged is

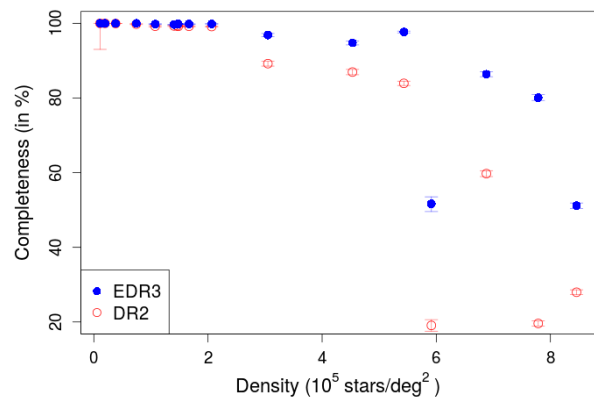


**Fig. 6.** Improvement of the *Gaia* completeness at  $G = 20$  mag versus some OGLE fields of different stellar densities from *Gaia* DR2 (red) to *Gaia* EDR3 (blue).

whether spuriously resolved single sources are at play. We notice that below  $0''.4$ , as many as 74% of the pairs are composed of 2p solutions, making it difficult to judge if they are genuine. For separations between  $0''.4$  and  $0''.5$ , the pairs of 2p solutions constitute only 40%.

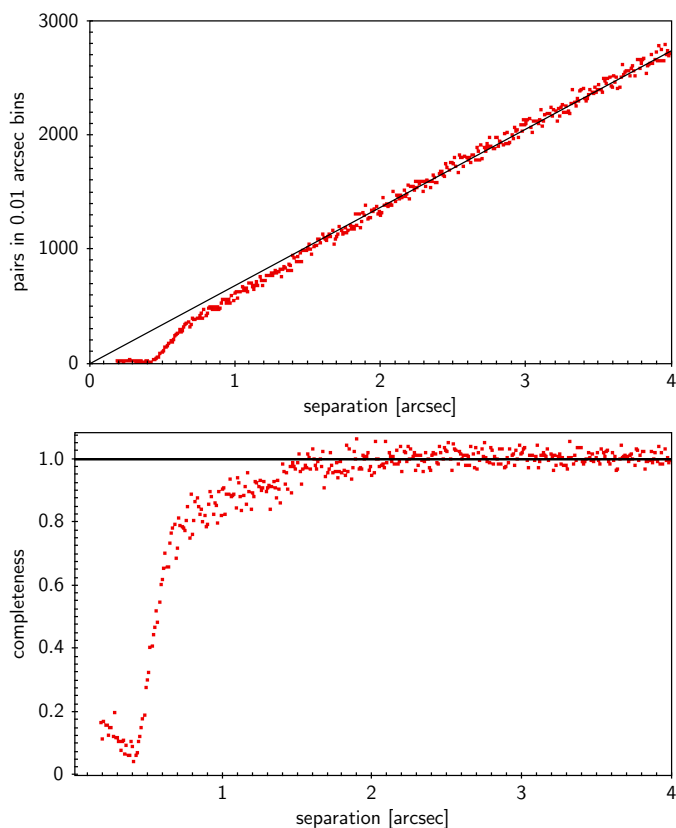
Figure 8 shows the improvement in the spatial resolution of *Gaia* EDR3 using the Washington Double Star Catalog (WDS; Mason et al. 2001). It confirms again that incompleteness is severe below  $0''.7$ , but it has improved substantially when compared to *Gaia* DR2.

#### 2.4. Completeness in crowded regions: Globular clusters

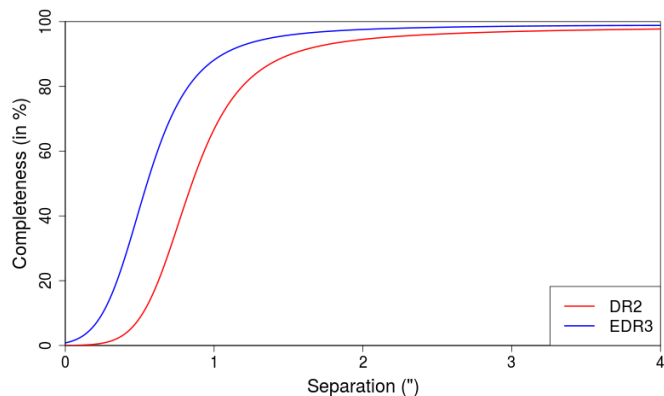
As already mentioned, the *Gaia* instrument has a limited capacity for observing very dense areas, and sources in these fields will get fewer observations and the limiting magnitude will be brighter. We derive the completeness in a few globular clusters which have various levels of crowding. The procedure and the sample are the same as described in Arenou et al. (2018). *Gaia* EDR3 data are compared with the catalogue of HST photometry by Sarajedini et al. (2007). We recall that the completeness of HST data is derived using crowding experiments and is higher than 90% in the whole *Gaia* range.

Table A.1 in Appendix A presents the results for the inner and outer regions of the cluster sample and shows the combined completeness of the astrometry and the photometry. Since, by construction, the *Gaia* photometry is only published for sources with an astrometric solution, the photometric completeness cannot be higher than the astrometric completeness. It can, however,





**Fig. 7.** *Top:* Histogram of source pair distances in a circular field of radius  $0.5^\circ$  centred at  $(l, b) = (330^\circ, -4^\circ)$  with a line showing the expected relation for a random distribution of the sources. *Bottom:* Normalised histogram using the expected relation.



**Fig. 8.** Improvement of the completeness (in percent) of visual double stars from the WDS catalogue as a function of the WDS separation between components from *Gaia* DR2 (red) to *Gaia* EDR3 (blue).

be lower, in particular in high density regions for the  $G_{BP}$  and  $G_{RP}$  photometry. Since this photometry is derived from dispersed images, crowding affects these measurements much more than astrometric measurements and  $G$  band photometry. We found that in globular clusters, a percentage of about 20%-30% of stars having five or six parameter solutions do not have  $G_{BP}$  and  $G_{RP}$  magnitudes. One of the worst cases is NGC 6809 where the percentage of stars without  $G_{BP}$  and  $G_{RP}$  is of 37%. Because of the lower level of crowding, open clusters are more favourable cases.

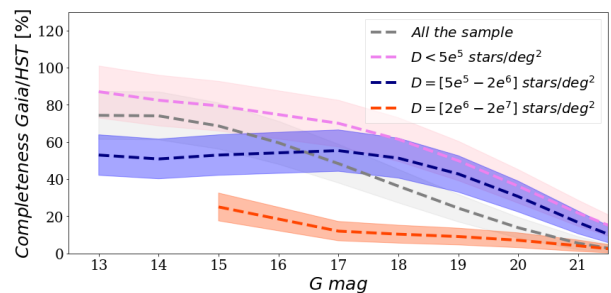


**Fig. 9.** Global completeness as a function of  $G$  for the whole sample of globulars (grey line). Pink, blue, and orange lines indicate the completeness in different density ranges  $D$ . The shaded areas indicate the uncertainties

In general, the percentage of stars without  $G_{BP}$  and  $G_{RP}$  is of the order of 1%-3%.

In globulars, the completeness is still at the 60% level for  $G \sim 19$  mag when the density is of the order of  $10^5$  stars/sq deg. The completeness is higher than 20% at  $G \sim 17$  mag when the density is lower than a few  $10^7$  stars/sq deg. At the faint end, in favourable cases, the completeness is still at the 80% level at  $G \sim 20$  mag (see Fig. 9). Inner and outer regions of the globulars have very different levels of completeness. For instance, in NGC 5053, the completeness in the inner and outer regions are very similar and quite high (60% at  $G \sim 20$  mag); in NGC 2298, the inner and outer regions have a very different level of completeness. In the inner region, the completeness is about 10% at  $G \sim 20$  mag, and 60% in the outer region. In the very crowded NGC 5286, the completeness in the inner region is 20% at  $G \sim 17$  mag. However, the completeness level is still variable for similar densities and magnitudes, depending on the number of observations among others (see Fig.9).

## 2.5. High proper motion stars

*Gaia* DR2 contained 951 sources with a proper motion above  $1000 \text{ mas yr}^{-1}$  and 3726 with motions above  $600 \text{ mas yr}^{-1}$ . The corresponding numbers for *Gaia* EDR3 are 633 and 2729, respectively, which is about 30% fewer. At first glance, this may look disturbing, but the fall is largely explained by spurious solutions in *Gaia* DR2 having been weeded out. This point is illustrated in Fig. 10. The top panel shows the 3 280 360 *Gaia* DR2 proper motions above  $50 \text{ mas yr}^{-1}$  against the parallax. There is a large population of negative parallaxes and also parallaxes approaching two arcseconds in absolute value. Conditions that trigger a spurious solution with a negative parallax, such as an unresolved duplicity, may equally well produce a spurious solution with a positive parallax as demonstrated by the overall symmetrical appearance. We return to this point in Sect. 3.2. The lower panel shows the corresponding plot for *Gaia* EDR3 with 3 273 397 sources, that is to say 6963 fewer. This plot has a better appearance with much fewer negative parallaxes. In particular, there are no more negative parallaxes for sources with proper motions above  $300 \text{ mas yr}^{-1}$ . Sources with a proper motion higher than  $1000 \text{ mas yr}^{-1}$  must – in the great majority – be relatively nearby and will only very rarely have a parallax below  $10 \text{ mas}$  lest their tangential velocity become unrealistically large. We can therefore safely assume that solutions giving negative parallaxes are mostly spurious for these large proper motion cases. In *Gaia* DR2, 175 of the 951 sources with large proper motions had a negative parallax and if we assume that a similar

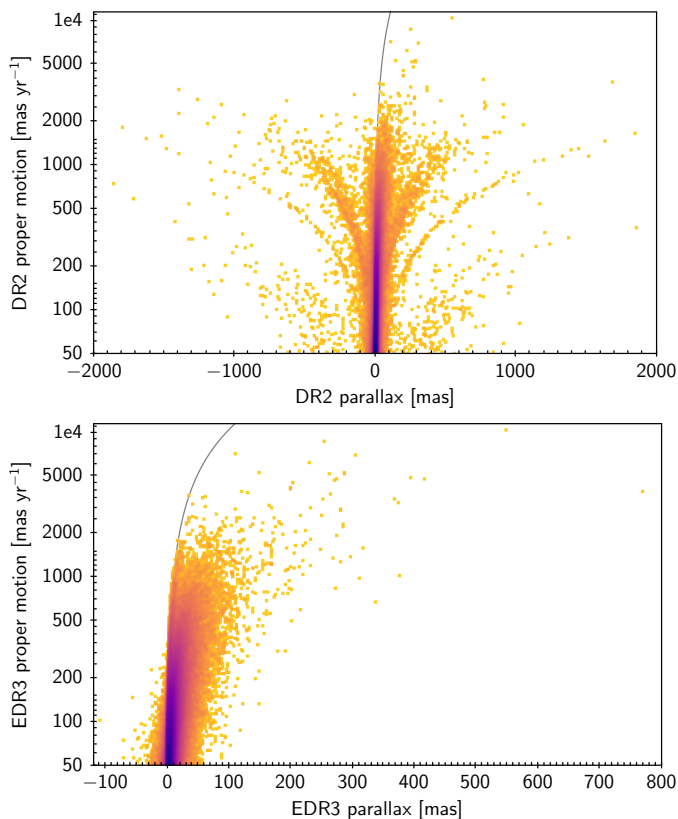


**Fig. 10.** Proper motion versus parallax for large proper motions. *Top:* In *Gaia* DR2. *Bottom:* In *Gaia* EDR3. The grey line shows the locus of tangential velocity  $500 \text{ km s}^{-1}$ .

number had a spurious positive parallax, we are down to about 600 good solutions. This is a number that compares favourably with the 633 such sources in *Gaia* EDR3. While it is possible to estimate the number of spurious solutions in *Gaia* DR2, it is not easy to identify which ones they are. We note that this improvement holds for high proper motion sources because they benefit more from the longer mission duration. We examine sources of lower proper motion in Sect. 3.2.

Comparing high proper motion stars with SIMBAD, we find that 8% of the SIMBAD stars with a proper motion higher than  $600 \text{ mas yr}^{-1}$  are missing in *Gaia* EDR3. Those are mostly stars with only a 2p solution in *Gaia* EDR3 and stars outside *Gaia*'s magnitude range, and a few show duplicated entries in *Gaia* EDR3.

### 2.6. Sources without parallax and proper motion

As many as 344 million sources have only a position published from the astrometric solution and neither parallax nor proper motion. The requirements for maintaining a full astrometric solution are detailed in Lindegren et al. (2020b). A source must, as mentioned, have at least nine visibility periods, the formal uncertainties must be sufficiently small, and the source must be brighter than  $G = 21 \text{ mag}$  according to the photometry available at the time of the astrometric processing, that is in *Gaia* DR2. The majority of the 2p sources have simply too few observations and will obtain a full solution in later releases.

If we look specifically at sources brighter than 19 mag, where the completeness is high, we have 8.8 million 2p solutions out of 575.9 million sources, that is 1.5%. This is a

clear improvement over *Gaia* DR2, which contained 13.8 million 2p solutions among 568.1 million sources, that is 2.4%. For these brighter sources, the problem is only the lack of observations for less than half of them. The rest have, for a large part, a problem with a close neighbour. This follows from the various indicators in the catalogue, such as `ipd_frac_odd_win`, which indicates observation window conflicts for wider pairs, `ipd_frac_multi_peak`, indicating resolved, closer pairs and `ipd_harmonic_gof_amplitude`, indicating asymmetric images for the closest pairs. The processing approach in *Gaia* EDR3 did not intend to resolve these pairs.

### 3. Astrometric quality of *Gaia* EDR3

The astrometric solution for *Gaia* EDR3, cf. Lindegren et al. (2020b), is based on 33 months of observations as compared to the 21 months for *Gaia* DR2. Therefore, there are reasons to not only expect a much improved precision, but also a much better ability to disentangle proper motions and parallaxes even for sources where (some) transits are biased by a close neighbour.

As already mentioned, there are three flavours of astrometric solutions in *Gaia* EDR3: either 2p, with only a position, 5p, with also parallax and proper motion, and finally 6p, where also a pseudo-colour is derived. The latter category encompasses the faintest sources and sources without a known colour in *Gaia* DR2 or with a clearly biased colour. Therefore, the more accurate astrometric solutions are those with five parameters (5p). This is partly the case because of the correlations introduced by deriving a colour from the astrometric measurements, in part because the photometric colour is missing precisely for the sources observed in the more difficult conditions, for example, in crowded areas or with a brighter source in the vicinity. Here, we concentrate on the 5p and 6p solutions, which are the ones of more interest.

We test the astrometry with an emphasis on the parallaxes. Here, large negative values reveal the presence of spurious solutions; distant objects such as quasars (QSOs) are suited for testing the parallax zero point; and star clusters and binaries, with sources located at nearly the same distance, are ideal for finding magnitude and colour dependent parallax errors. For the parallax precision, we use the negative wing of the parallax distribution. For proper motions, star clusters and binaries are again ideal when looking for magnitude dependent errors.

Lindegren et al. (2020a) calculated a parallax zero point correction depending on the magnitude, colour, and ecliptic latitude, using different tracers (QSOs, red clump stars, stars from the Large Magellanic Cloud (LMC), binaries). The paper provides recipes for correcting the zero point error, at least in a statistical sense. We therefore also look into the effect of applying these corrections.

#### 3.1. Imprints of the scanning law

The scanning law for *Gaia* (Gaia Collaboration et al. 2016, sect. 5.2) specifies the direction of the spin axis of the spacecraft – and thereby also the great circle being observed – as a function of time. The axis precesses around the Sun at an angle of  $45^\circ$  with a period of 63 days, thereby creating a characteristic pattern in the number of transits across the sky with high values at  $\pm 45^\circ$  ecliptic latitude and in loops in between.

Figure 11 shows the average separation between sources in *Gaia* EDR3 and their counterparts in *Gaia* DR2, taking *Gaia* EDR3 proper motions into account. Only separations below 10 mas and sources with a known proper motion have been

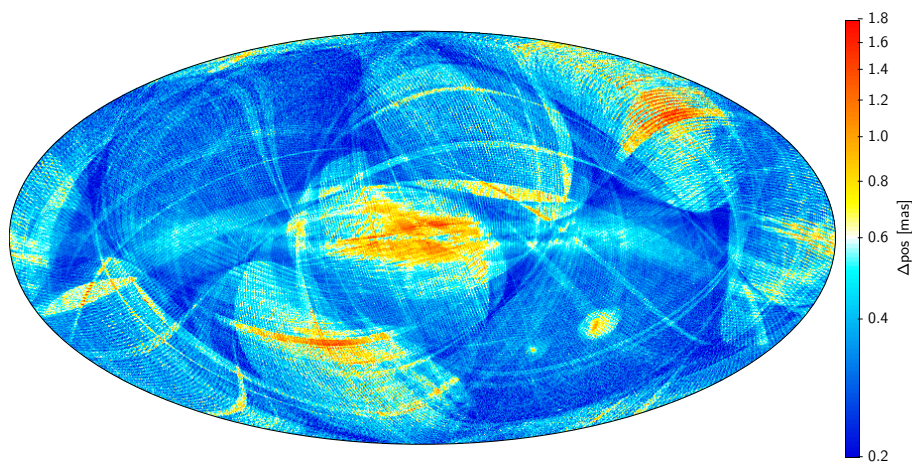


**Fig. 11.** Map in Galactic coordinates of the mean positional difference between *Gaia* EDR3 and *Gaia* DR2, having propagated the *Gaia* EDR3 positions to the epoch of *Gaia* DR2.

used (1458.7 million sources). The map shows that the discrepancy is normally at the sub-mas level, but there are also specific areas of the sky where they approach 2 mas. On the one degree scale, there is a clear scan-law pattern. The plot is dominated by very faint sources and does not reflect the performance in the bright end. Although it cannot be deduced from the map itself, we believe that it largely shows positional errors of *Gaia* DR2.

Figure 12 shows the remaining chequered-pattern systematics in the parallaxes due to the *Gaia* scanning law in the direction of the LMC and of the Galactic centre, where the parallaxes are small and homogeneous enough so that variations in the median values merely reflect the parallax errors. The systematics for 6p are larger than for 5p, but they have otherwise decreased together with the chequered-pattern since DR2 (cf. Arenou et al. 2018, fig. 13).

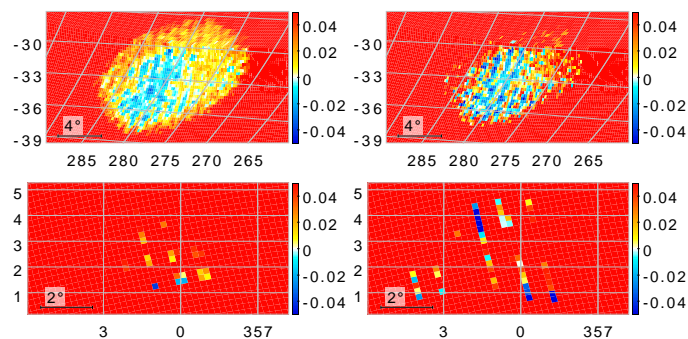


**Fig. 12.** Maps in Galactic coordinates of median parallaxes in the direction of the LMC (*top*) and Galactic centre (*bottom*) for 5p (*left*) and 6p (*right*) solutions. To increase the contrast, the represented parallax range is  $[-0.05, 0.05]$  mas, although the median parallax in most of the field is above 0.05 mas.

### 3.2. Spurious astrometric solutions

An astrometric solution for a source is derived from a cluster of transits covering nearly three years and associated with the same source identifier. It is a fundamental assumption that the image parameters for each of these transits all refer to the same astrophysical source. Ideally, this is an isolated point source, but it could also be the photocentre of an unresolved pair. For close source pairs, this assumption breaks down. Depending mainly on the scan angle, different transits may then give image parameters for one or the other source, and sometimes for the photocentre.

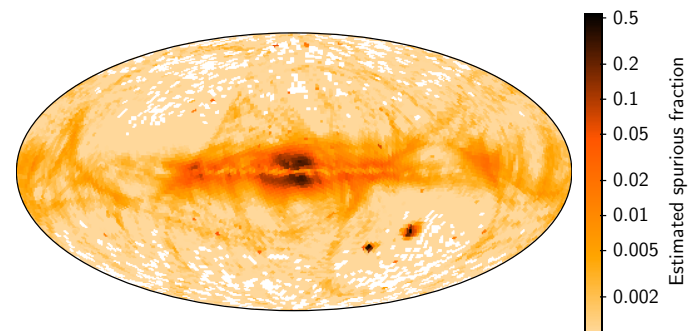
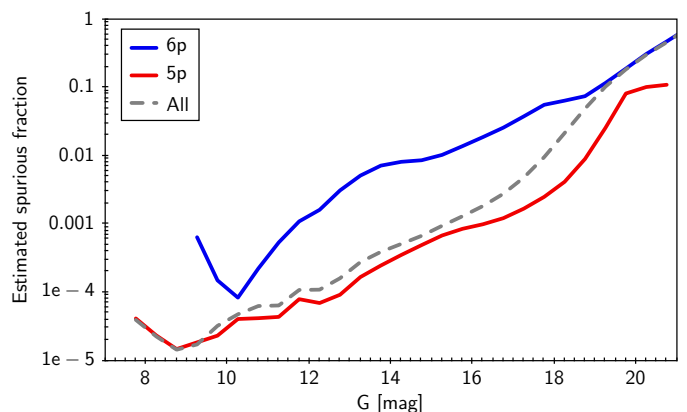


**Fig. 13.** Estimated fraction of spurious solutions for sources where the formal uncertainty is at least five times smaller than the parallax. *Top*: The fraction by  $G$  for the whole catalogue (dashed line) as well as separately for 5p (lower, red line) and 6p (upper, blue line) solutions. *Bottom*: Skymap of the fraction for the whole catalogue in Galactic coordinates.

In these cases, there is a risk that the astrometric solution will produce meaningless proper motions and parallaxes. Here, we call these spurious astrometric solutions. Several different quality indicators for the solution help to identify such cases, cf. Lindgren et al. (2020b).

A common way of selecting reliable astrometric solutions – in particular parallaxes – is to use only parallaxes larger than some apparently safe value or only parallaxes much larger than their estimated uncertainties. At first glance, it does appear safe to use only parallaxes with relatively small errors, for example with `parallax_over_error`  $> 5$ . There are 192.21 million sources in *Gaia* EDR3 with such good parallaxes. We use the limit of five as an illustrative example and not as a recommen-



dation. The point is simply that the number of negative parallaxes fulfilling the `parallax_over_error < -5` condition is expected to be extremely small for a Gaussian error distribution.

Formal uncertainties can, however, be misleading. They are based on the assumption that the source is undisturbed and can be properly described using a five-parameter model. This is normally true, but far from always. One way to find spurious solutions is to count the fraction of very negative parallaxes, for example for the present example smaller than minus five times the formal uncertainty. There are 3.04 million sources with `parallax_over_error < -5`. These solutions are clearly spurious.

We can reasonably assume that a disturbance giving rise to a negative (spurious) parallax, for example image parameters affected by duplicity or crowding, could just as well have produced a spurious solution with a positive parallax and with roughly the same probability. We therefore get a conservative estimate of the number of spurious, positive parallaxes by counting the negative ones. Needless to say, disturbances can also be so small that they merely produce slightly wrong positive parallaxes, but these cases are harder to find.

We can therefore say that among the 192.21 million significant, positive parallaxes, of the order of 3.04 million are spurious, that is to say 1.6% of this ‘good’ sample. As illustrated in Fig. 13 (upper panel), the spurious fraction, determined in this way, strongly depends on magnitude and is much higher for 6p solutions than for 5p ones. We recall here that 6p solutions are used for sources where some circumstances prevented good  $G_{BP}$  and  $G_{RP}$  photometry from being determined in the processing for *Gaia* DR2. It is reasonable to assume that it is these very circumstances that have also led to the spurious astrometry rather than the inclusion of a sixth parameter. The lower panel of Fig. 13 shows that areas such as the LMC and the Galactic centre have a particularly high fraction of spurious solutions. This is very likely caused by crowding. When evaluating parallaxes for a particular sample of sources, where only positive parallaxes are selected, we therefore recommend to also select a similar sample, but with negative parallaxes in order to evaluate the likely fraction of spurious results.

Thanks to the better angular resolution in *Gaia* EDR3, the number of spurious solutions has decreased substantially since *Gaia* DR2. This can be illustrated with a proper motion diagram near the Galactic centre (Fig. 14). In this region of the ecliptic, with a small number of visibility periods, there are mostly two perpendicular scanning directions which are now barely visible, but which clearly appeared with spurious proper motions in the corresponding *Gaia* DR2 figure (Arenou et al. 2018, fig. 11b). With many half-resolved doubles in this very dense region, distorted image parameters can explain a large number of spurious solutions, that is to say solutions, which have large proper motion errors in *Gaia* DR2.

Compared to *Gaia* DR2, the dispersion of the proper motions in Fig. 14 is a factor  $> 3$  smaller, so that one could wonder whether spurious solutions are still present. Here the `ipd_gof_harmonic_amplitude`<sup>5</sup> parameter can be of help: Values above 0.1 for sources with `ruwe`<sup>6</sup> larger than 1.4 characterise resolved doubles, which have not been correctly handled yet. Using this parameter as an explanatory variable on Fig. 14 (upper panel), we conclude that the corona

<sup>5</sup> `ipd_gof_harmonic_amplitude` indicates the level of asymmetry in the image, cf. Table B.1.

<sup>6</sup> `ruwe` is the renormalised unit weight error (for astrometry) given in the *Gaia* archive.

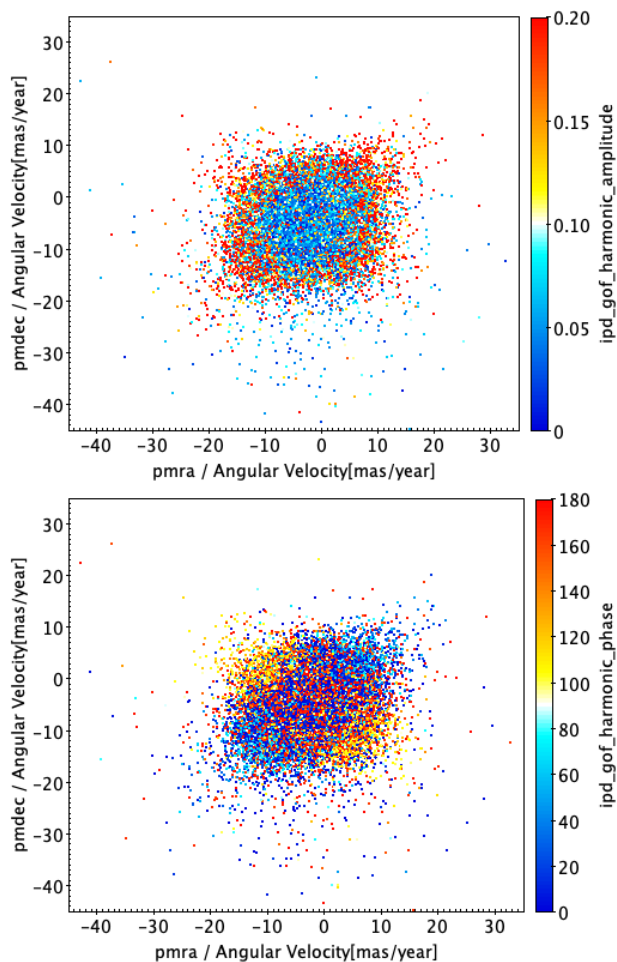


**Fig. 14.** Proper motion diagram of sources near the Galactic centre within a  $0.5^\circ$  radius. *Top:* Colour-coded by `ipd_gof_harmonic_amplitude`. *Bottom:* Coded by `ipd_gof_harmonic_phase`. Reddish points in the top panel reveal potentially spurious solutions.

of relatively large proper motions can be spurious, since the `ipd_gof_harmonic_phase`<sup>7</sup> in Fig. 14 (lower panel) suggests that these sources were partly resolved along the two principal scanning directions.

### 3.3. Large-scale systematics

The quasars are distant enough so that the DR3 measured parallax directly gives the astrometric error, thus QSOs can be used to estimate the large-scale variation of the parallax systematics. The QSO sample used is mostly a subset from outside of the Galactic plane of the sources listed in the table `agn_cross_id` published as part of the *Gaia* Archive for EDR3. The sample was filtered from potential  $5\sigma$  outliers in parallax or proper motion and from potential non-single objects using: `ruwe < 1.4` and `ipd_frac_multi_peak  $\leq$  2` and `ipd_gof_harmonic_amplitude < 0.1`.

Median parallaxes were computed in overlapping regions of radius  $5^\circ$  having at least 20 QSOs and are shown in Fig. 15. Compared to the similar plot done for *Gaia* DR2 (Arenou et al. 2018, fig. 15), the improvement in the top panel of Fig. 15 is very

<sup>7</sup> `ipd_gof_harmonic_phase` indicates the orientation of an asymmetric image.



clear for the 5p solutions. A slight north-south asymmetry appears with, for example, parallaxes below  $\beta < -30^\circ$  being about  $8 \mu\text{as}$  more negative than those above  $\beta > 30^\circ$ . Applying the zero point correction from Lindegren et al. (2020a) removes this asymmetry (see bottom panel of Fig. 15); some east-west asymmetry along the ecliptic of a few  $\mu\text{as}$  may, however, remain. It is more difficult to conclude about the 6p solutions: They represent only 20% of the QSO sample and have larger uncertainties, so the amplitude of the variations may be more related to random errors than to systematics.

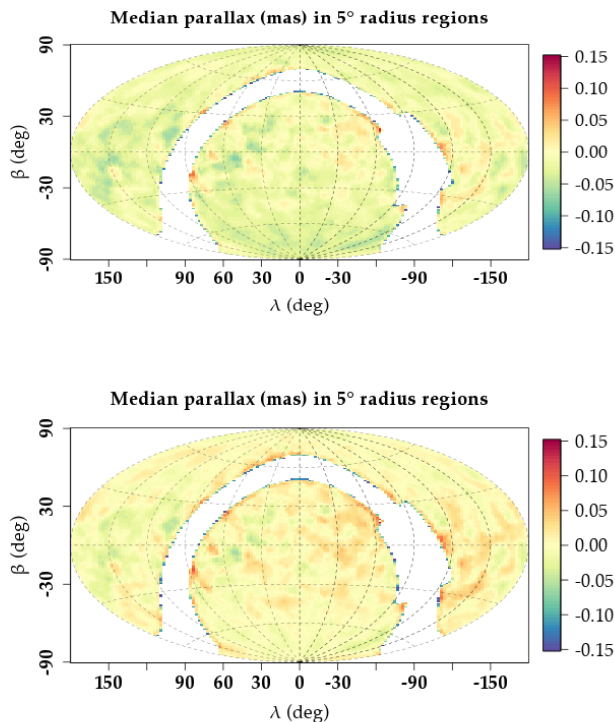


**Fig. 15.** Maps in ecliptic coordinates of the variations of QSO parallaxes (mas) in  $5^\circ$  radius fields. *Top*: 5p solution. *Bottom*: 5p with zero point correction.

### 3.4. Comparison to external data

We compared the *Gaia* EDR3 parallaxes with external catalogues described in detail in the *Gaia* EDR3 online documentation.<sup>8</sup> Those are the same as used in Arenou et al. (2018), except that we updated the APOGEE catalogue to the DR16 version (Ahumada et al. 2020), the ICRF catalogue to its third realisation (Charlot et al. 2020), and added dSph members. We show the summary of the results in Table 1 without and with the parallax zero point correction of Lindegren et al. (2020a) applied. The correction significantly improves the parallax differences, the exceptions being the LMC and SMC (Small Magellanic Cloud) stars sub-selected by their *Gaia* DR2 radial velocities, which are bright, and the two largest dSph of our sample, Sculptor and Fornax. The parallax difference with HIPPARCOS is within the expected HIPPARCOS parallax zero point uncertainty (up to 0.1 mas,

<sup>8</sup> [https://gea.esac.esa.int/archive/documentation/GEDR3/Catalogue\\_consolidation/chap\\_cu9val/sec\\_cu9val\\_944/](https://gea.esac.esa.int/archive/documentation/GEDR3/Catalogue_consolidation/chap_cu9val/sec_cu9val_944/)

Arenou et al. 1995), but a correlation of the parallax difference with the magnitude is seen for HIPPARCOS stars brighter than  $G = 6$  mag. The jump in the parallax zero point at  $G \sim 13$  mag (Lindegren et al. 2020a) is seen in the APOGEE comparison and removed by the application of the parallax zero point correction. The variation in the QSO parallax with the magnitude for 5p solutions was also removed by the parallax zero point correction. A correlation of the parallax zero point with the pseudo-colour is seen in the dSph, in particular in Fornax, which was reduced but not fully removed by the parallax zero point correction of Lindegren et al. (2020a).

Concerning the proper motions, we looked in particular at the difference between the *Gaia* proper motion and the proper motion derived from the positions of *Gaia* and HIPPARCOS. By construction (sect. 4.5 of Lindegren et al. 2020b), the global rotation between those proper motions, seen in *Gaia* DR2 (Lindegren et al. 2018b; Brandt 2018), is not present anymore. However, a variation of this rotation with magnitude and colour is still present but smaller than for *Gaia* DR2 (the maximum variation reaching  $0.1 \text{ mas yr}^{-1}$  for bright or red sources). We note that between *Gaia* and HIPPARCOS proper motions, a global rotation is still present with  $w = (-0.120, 0.173, 0.090) \pm 0.005 \text{ mas yr}^{-1}$ . This is a deviation well within the estimated accuracy of the HIPPARCOS spin.

### 3.5. Comparison to a Milky Way model

We compared the astrometric data to that of the GOG20 simulation in order to investigate potential systematic errors. This was done by computing the median of the parallaxes and the median of the proper motions in each healpix bin of the sky map for all of the data and the model. The comparison for the median parallaxes are shown in Fig. 16 as a function of magnitude for *Gaia* EDR3, *Gaia* DR2, and the GOG20 simulation.

The median parallaxes are generally in very good agreement between *Gaia* EDR3 and GOG20, specially at magnitudes larger than ten. However, there is a systematic difference which, in absolute value, depends on magnitude, and it is quite high on the bright side and more than 1 mas. This systematic difference between the data and model simulation is a bit reduced in *Gaia* EDR3 compared to *Gaia* DR2. At  $G > 10$  mag, the difference goes below 0.1 mas. Regarding the proper motions, the model and data present approximately similar patterns in all magnitude ranges. However, there are systematics, as was already noted in the validation of *Gaia* DR2. Overall, *Gaia* EDR3 data are as expected from our knowledge of the Galactic kinematics up to very faint magnitudes and it is probably the model which suffers from systematics, or it does not account for asymmetries. Indeed, we note that the change of kinematics prescriptions from GOG18 to GOG20 generally allows for a better agreement with the data.

### 3.6. Astrometric zero point and precision of the parallaxes from cluster analysis

The zero point of the parallaxes was verified using three external reference catalogues of open clusters. We made use of Dias et al. (2014) (hereafter DAML), Kharchenko et al. (2013) (hereafter MWSC), and finally Cantat-Gaudin et al. (2020) based on *Gaia* DR2 parallaxes. We selected the most suitable clusters for this aim: a selection of about 200 clusters with well known parameters (hereafter best sample) for a total of about 70 000 stars; and a wider sample of 2043 clusters including 250 000

**Table 1.** Summary of the comparison between the *Gaia* parallaxes and the external catalogues.

Catalogue	Nb	Outliers	$\langle G \rangle$	$\varpi$ difference	$\varpi_{cor}$ difference	$\varpi_{cor}$ uwu
HIPPARCOS	62484	0.15%	8.2	$-0.089 \pm 0.003$	$-0.068 \pm 0.002$	$2.4 \pm 0.4$
VLBI	40	8%	8.3	$-0.01 \pm 0.01$	$0.02 \pm 0.01$	$2.0 \pm 0.4$
HST	49	27%	12.2	$0.01 \pm 0.02$	$0.03 \pm 0.02$	$1.9 \pm 0.3$
RECONS	427	3%	12.6	$-0.8 \pm 0.06$	$-0.8 \pm 0.06$	$1.54 \pm 0.06$
<i>Gaia</i> Cepheids	1372	1%	15.7	$-0.028 \pm 0.0007$	$0.006 \pm 0.0007$	$1.22 \pm 0.02$
<i>Gaia</i> RRLyrae	318	2%	18.1	$-0.030 \pm 0.008$	$-0.001 \pm 0.008$	$1.04 \pm 0.05$
APOGEE	3453	2%	18.6	$-0.046 \pm 0.003$	$-0.007 \pm 0.003$	$1.19 \pm 0.02$
SEGUE Kg	2491	0.04%	17.3	$-0.029 \pm 0.002$	$0.004 \pm 0.001$	$1.07 \pm 0.02$
LMC	52795	0.7%	19.2	$-0.023 \pm 0.0003$	$0.003 \pm 0.0003$	$1.3 \pm 0.004$
LMC Vr	318	1.6%	12.8	$-0.004 \pm 0.001$	$0.015 \pm 0.001$	$2.17 \pm 0.09$
SMC	26480	1.3%	16.4	$-0.0255 \pm 0.0002$	$0.0055 \pm 0.0002$	$1.26 \pm 0.006$
SMC Vr	114	9.6%	12.5	$-0.006 \pm 0.001$	$0.016 \pm 0.001$	$1.5 \pm 0.1$
Draco	427	0%	19.3	$-0.024 \pm 0.005$	$0.0002 \pm 0.006$	$1.09 \pm 0.04$
Sculptor	1286	0.08%	19.1	$-0.011 \pm 0.005$	$0.015 \pm 0.004$	$1.09 \pm 0.03$
Sextans	528	0%	19.4	$-0.015 \pm 0.01$	$0.01 \pm 0.01$	$1.00 \pm 0.03$
Carina	865	0%	19.8	$-0.014 \pm 0.005$	$0.012 \pm 0.005$	$1.03 \pm 0.02$
Antlia II	159	0%	18.9	$-0.025 \pm 0.012$	$-0.0006 \pm 0.01$	$0.89 \pm 0.05$
Fornax	2660	0.6%	18.8	$-0.013 \pm 0.003$	$0.011 \pm 0.003$	$1.16 \pm 0.03$
LeoII	185	0%	19.8	$0.005 \pm 0.03$	$0.02 \pm 0.03$	$1.0 \pm 0.05$
LeoI	328	0.3%	19.6	$-0.063 \pm 0.02$	$-0.05 \pm 0.02$	$1.11 \pm 0.04$
all dSph	7174	0.3%	19.0	$-0.017 \pm 0.002$	$0.008 \pm 0.002$	$1.09 \pm 0.01$
ICRF3	3172	0.06%	18.9	$-0.023 \pm 0.002$	$0.001 \pm 0.002$	$1.10 \pm 0.01$
LQRF	8231	0.03%	19.1	$-0.024 \pm 0.0006$	$-0.0015 \pm 0.0006$	$1.063 \pm 0.003$
RFC2016cnoU	3705	0.05%	18.9	$-0.022 \pm 0.002$	$0.002 \pm 0.002$	$1.090 \pm 0.01$

**Notes.** We present the total number of stars used in the comparison (Nb) as well as the percentage of outliers excluded (at  $5\sigma$ , in violet if higher than 10%) as well as the median  $G$  of the sample. The parallax differences ( $\varpi_G - \varpi_E$ , in mas), the parallax difference with the correction of Lindegren et al. (2020a) applied ( $\varpi_{cor}$ ) and the unit-weight uncertainty (uwu) that needs to be applied to the uncertainties to adjust the differences are indicated in violet when they are significant (p-value limit: 0.01) and higher than  $10 \mu\text{as}$  for the parallax difference and 10% for the uwu. For the HIPPARCOS catalogue, in addition to the uwu, a systematic uncertainty of 0.5 mas has yet to be quadratically added.

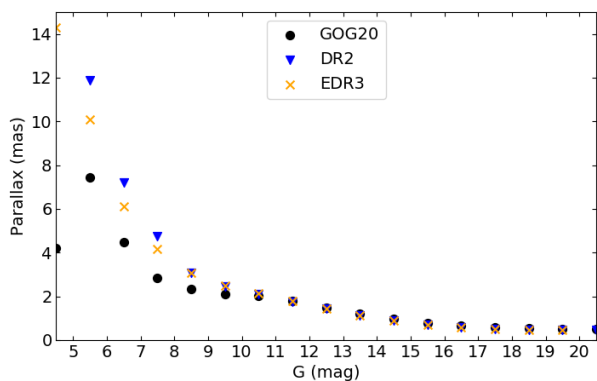


**Fig. 16.** Parallaxes averaged among healpix bins over the whole sky as a function of magnitude for *Gaia* EDR3 (orange crosses), GOG20 (black circles), and *Gaia* DR2 (blue triangles).

stars (hereafter whole sample). The best sample is the same sample that was already used to validate *Gaia* DR2 in Arenou et al. (2018). The whole sample is based on Cantat-Gaudin et al. (2020) cluster identification and parameters. Cluster members for this analysis were obtained using *Gaia* EDR3 proper motions selected within one  $\sigma$  from the mean value. Clusters closer

than 1000 pc show an intrinsic internal dispersion in the parallaxes and are not suitable for estimating the zero point. When we used clusters located farther away, we derived an average zero point difference ( $\varpi_{Gaia} - \varpi_{reference}$ ) =  $-0.059$  mas for MWSC and  $-0.091$  mas for DAML, but with a large  $\sigma \sim 0.2$  mas. Looking at the trends of the zero point with colour and magnitude, we find a complex pattern. In Fig. 17, we plotted the differential parallax to the cluster median  $\Delta_{\varpi}$  for the whole sample of clusters located farther than 1000 pc, which were normalised and not normalised to the nominal parallax uncertainties. We note that  $\Delta_{\varpi}$  gives an indication about zero point changes. When plotted versus  $G$ , we detected discontinuities in the zero point at  $G \sim 11, 12,$  and  $13$  mag. Strong variations are evident for stars bluer and redder than  $G_{BP} - G_{RP} \sim 0.9$  mag. Figure 17 (right panel) presents the variation of  $\Delta_{\varpi}$  in the colour-magnitude diagram, showing a number of discontinuities and a complex pattern. At faint magnitudes, red stars have a higher dispersion; however, the effect can be due to the less reliable membership, while at red colours, the large variations can reflect poor statistics. When divided by the nominal uncertainty, these patterns are still present with a reduced amplitude, implying that nominal uncertainties on the parallax do not account for the zero point variation, that is to say nominal uncertainties are underestimated.

Clusters are very good targets to test the quality of the parallax correction from Lindegren et al. (2020a) since all the stars are expected to have the same parallax. In addition, clusters can

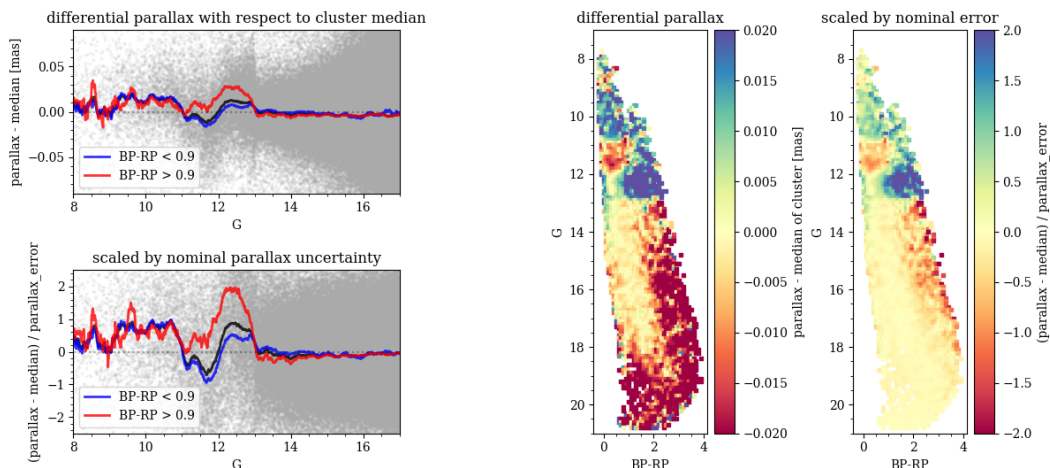


**Fig. 17.** *Left:*  $\Delta_{\varpi}$  (top) and scaled to the nominal uncertainties  $\Delta_{\varpi}$  (bottom) versus  $G$  for the whole sample of clusters. The solid lines show the LOWESS (locally weighted scatterplot smoothing) of the stars bluer (redder) than  $G_{\text{BP}} - G_{\text{RP}} = 0.9$  (blue and red lines), while the black line is for the whole sample. *Right:* CMD of the whole sample where the colour shows the differential parallax to the median.

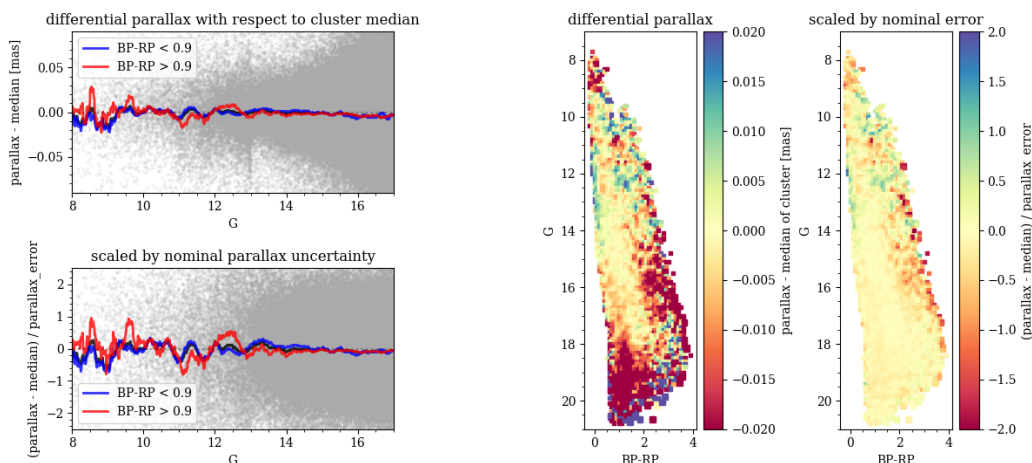


**Fig. 18.** *Left:*  $\Delta_{\varpi}$  (top) and the scaled  $\Delta_{\varpi}$  (bottom) versus magnitude for the whole sample after the correction to the parallax zero point is applied. The solid lines show the LOWESS of the stars bluer (redder) than  $G_{\text{BP}} - G_{\text{RP}} = 0.9$  mag (blue and red lines). The black line is the for the whole sample. *Right:* CMD of the whole sample where the colour shows the differential parallax to the median, and the analogous scaled to the nominal parallax uncertainties after parallax zero point correction (see text for details).

be found close to the Galactic plane, where no calibration tracers are located. This allows for an independent verification. We applied this correction to the cluster data, using the Matlab code<sup>9</sup> provided in the Lindegren et al. (2020a) paper.

The results are shown in Fig.18 where we plotted the  $\Delta_{\varpi}$  and the scaled  $\Delta_{\varpi}$ , that is to say the analogue was scaled to the nominal uncertainties on parallaxes as a function of the  $G$  magnitude, and finally the residuals to the median in the colour magnitude diagram. This correction reduces the dispersion inside the clusters at bright magnitudes and bluer colours, while at faint magnitudes ( $G > 18$  mag) or a redder colour, the dispersion is still high. The median values scaled to the nominal uncertainties are always  $< 1$ , which indicates that nominal uncertainties account for the residual variations. Clearly this positive result should be taken with caution. It refers to a specific range of colours and positions in the sky.

<sup>9</sup> A python code is distributed with *Gaia* EDR3 at <https://www.cosmos.esa.int/web/gaia/edr3-code>.

Finally, we compare the parallaxes of single stars in *Gaia* DR2 and *Gaia* EDR3 for the whole cluster sample. The median difference is  $(\varpi_{\text{Gaia DR3}} - \varpi_{\text{Gaia DR2}}) = 0.017$  mas (with 16th percentile =  $-0.047$  mas; 84th percentile =  $0.082$  mas) with a dependence on the magnitude.

### 3.7. Uncertainty of the astrometric parameters

We evaluate the actual precision of the astrometric parameters partly from parallaxes and proper motions of QSOs and of stars in the LMC and partly from deconvolution of the negative parallax tail. As discussed by Lindegren et al. (2018a), it is useful to describe the true external parallax uncertainty,  $\sigma_{\text{ext}}$ , as the quadratic sum of the formal catalogue uncertainty ( $\text{parallax\_error}$ ) times a multiplicative factor ( $k$ ) plus a systematic error ( $\sigma_s$ ),

$$\sigma_{\text{ext}}^2 = k^2 \sigma_i^2 + \sigma_s^2. \quad (1)$$



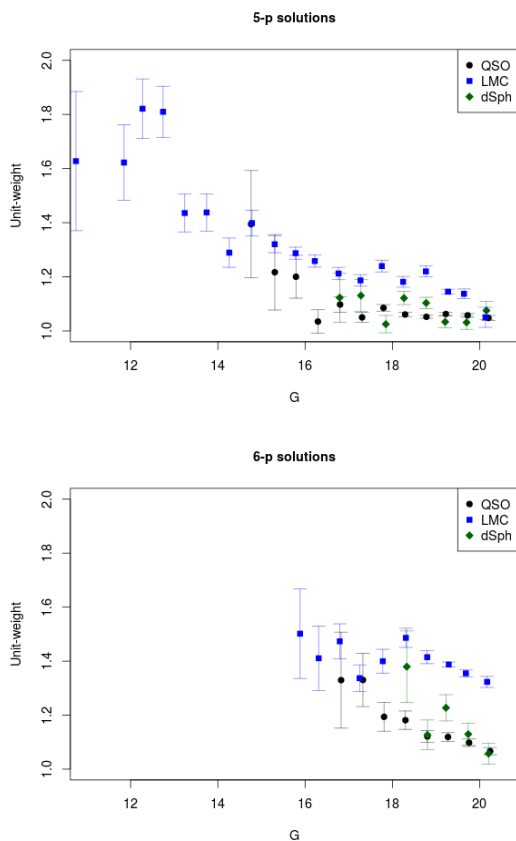


**Fig. 19.** Unit-weight uncertainty (uwu) that needs to be applied to the *Gaia* parallax uncertainties to be consistent with the residual distribution (after zero point correction and removing stars with  $\text{ruwe} < 1.4$ ) versus LQRF QSOs, LMC, and dSph stars for the 5p (top) and 6p (bottom) solutions, as a function of magnitude.

In addition to this, the catalogue uncertainties incorporate part of the excess noise of the solution when present. Consequently, large uncertainties typically correspond to both fainter sources and/or non-single stars.

### 3.7.1. Uncertainty of parallax and proper motion from distant objects

Similarly to what was found for *Gaia* DR2 by Arenou et al. (2018), QSOs show that the uncertainties are slightly underestimated and that this under-estimation increases with magnitude. The under-estimation is lower than for *Gaia* DR2 for the 5p solution, but larger for the 6p solution. This is seen for a parallax using the unit-weight uncertainty (uwu) in Fig. 19 and for proper motion using a  $\chi^2$  test in Fig. 20. The trend with magnitude is also seen with LMC stars, although the under-estimation of uncertainties is higher, as presented in Fig. 21, which is most probably due to the crowding. The increase in the under-estimation is also seen in the uwu presented in Table 1. The uwu reported is the  $k$  term of Eq. 1, assuming a negligible systematic error term ( $\sigma_s$ ) except for the HIPPARCOS comparison which is the only catalogue for which both terms could be clearly separated. The uwu and the residual  $R_\chi$  were computed after applying the parallax zero point correction of Lindegren et al. (2020a) and removing stars with  $\text{ruwe} > 1.4$ .

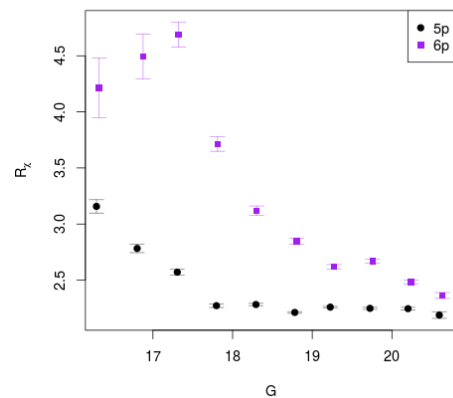


**Fig. 20.**  $\chi^2$  test of the LQRF QSOs proper motions as a function of  $G$  magnitude for the 5p (black circles) and 6p (purple squares) solution. The residual  $R_\chi$  should follow a  $\chi^2$  with 2 degrees of freedom. The correlation observed here is due to the underestimation of the uncertainties as a function of magnitude.

### 3.7.2. Parallax uncertainties by deconvolution

The ‘true’ dispersion of the parallaxes was estimated using a deconvolution method, which was applied on the negative tail of the parallaxes (see Arenou et al. 2017, sect. 6.2.1 for details), and the uwu ratio of the external over the internal uncertainty was computed. Figure 21 shows the uwu as a function of the catalogue uncertainties for several illustrative subsets and it can give insights into the underestimation factor, the systematics, and the contamination by non-single sources.

On the right side of the figure, the asymptotic uwu is mostly flat and it gives the multiplicative factor: It is about 1.05 for 5p solutions (improved from DR2), slightly more for very faint stars, 1.22 for 6p solutions, and larger for sources with non-zero excess noise or those in the LMC. While the uwu is in general slowly increasing with uncertainty due to the contamination by non-single sources, it increases sharply for sources brighter than 17 mag, most probably due to half-resolved doubles (as indicated by the average  $\text{ipd\_frac\_multi\_peak}$  or  $\text{ipd\_gof\_harmonic\_amplitude}$ ), which suggests that the uncertainties of these non-single bright stars are underestimated quite a bit. Then, the left part of the curves shows the influence of the systematics. As confirmed by other tests, the systematics have decreased compared to DR2, except for 6p solutions, and they are largest for sources with non-zero excess noise, which is due to either calibration errors or to perturbation of non-single stars.

### 3.8. Magnitude dependence from binary stars

One way to check the magnitude variations of the parallax zero point is to use resolved binary stars. When the period of the binary system is long enough, the proper motion of the two components is similar, or at least the differences are smoothed out when a large sample is used. Potential common proper motion pairs have been selected over the whole sky; this has been restricted to primaries up to  $G < 15$  mag and secondaries up to  $G < 18$  mag only: Selecting fainter secondaries would increase the fraction of optical doubles in dense fields too much, thus biasing the parallax differences. We computed the differences between the two components of their parallax and proper motion,

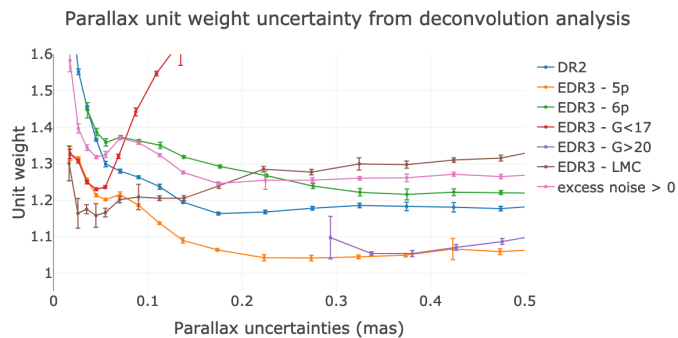


**Fig. 21.** Uwu of the parallaxes estimated by deconvolution versus `parallax_error` (mas) for several subsets: DR2 and EDR3 for 5p, 6p,  $G < 17$  mag,  $G > 20$  mag, LMC, and non-zero excess noise.

then the norm of this difference accounting for its covariance was determined, and a pair was considered as a true binary if this  $\chi^2$  had a p-value above 0.01 and the linear separation was below  $10^4$  au.

The differences of the parallax and proper motion between primary and secondary components are represented in the top panel of Fig. 22 versus the  $G$  magnitude of the primary. For  $12 < G < 13$  mag, a  $20 \mu\text{as}$  increase for the parallax zero point differences appears clearly, which was not present with DR2 parallaxes. A significant improvement is seen after the zero point correction from Lindegren et al. (2020a). Although within the uncertainty (below  $0.007$  mas, approximately constant), a small residual effect near  $G \approx 11.5$  mag or  $G \approx 13$  mag may perhaps still be present. It should not come as a surprise that these variations occur in the magnitude interval where there is a change in the gating scheme or in the window size (Lindegren et al. 2020a, sect. 2.1). For primaries brighter than 7 mag (middle panel of Fig. 22), the zero point may be more negative, as can also be seen using known WDS binaries.

We tested the consistency between the parallax of two components of wide physical binaries, which were selected from the WDS (separation larger than  $0.5''$  and flag 'V'). We again found how the magnitude dependence of the parallax zero point present in *Gaia* EDR3 is nicely removed by applying the parallax zero point correction of Lindegren et al. (2020a), thus confirming the results shown in Fig. 22 (middle panel). Similarly, following Kervella et al. (2019), we used their catalogue of Cepheids and RR Lyrae resolved common proper motion pairs to check the compatibility of their parallaxes. With the parallax zero point correction of Lindegren et al. (2020a), and opposite to the *Gaia* DR2 results for Cepheids, no systematic offset nor strong outlier (outside  $5\sigma$ ) were found.

While no variation appears for  $\mu_\delta$  in the bottom panel of Fig. 22, there is an increase of about  $0.01 \text{ mas yr}^{-1}$  at  $G = 13$  mag for  $\mu_{\alpha^*}$ . Although this may not look statistically significant (uncertainty  $\approx 0.007 \text{ mas yr}^{-1}$ ), this effect is probably real, as an empirical  $0.1$  mas rotation correction was applied to the proper motion system for  $G < 13$  mag (Lindegren et al. 2020b, sect. 4.5).

### 3.9. Pseudo-colour dependence

The 6p solutions derive both the astrometric parameters and the pseudo-colour. Although the correlation between the parallax and pseudo-colour is, in general, not large (top panel of Fig. 23), this nevertheless implies that (random or systematic) errors in the pseudo-colour translate into systematics on the par-

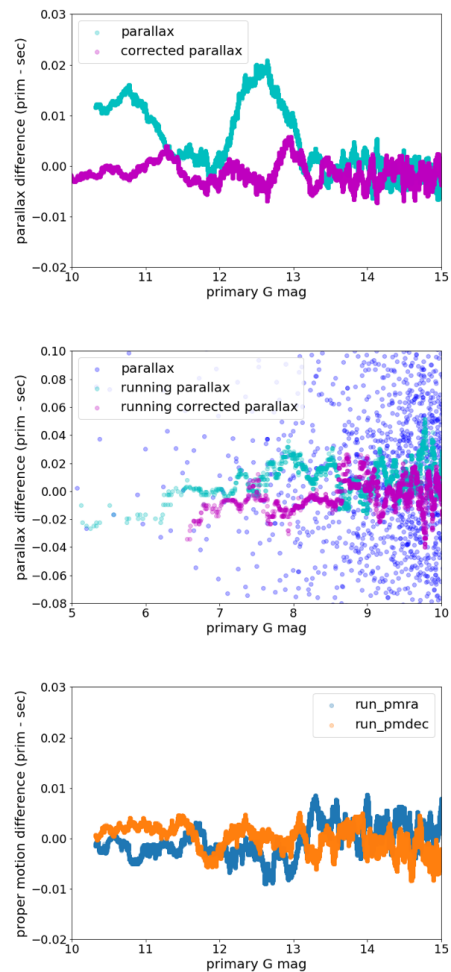


**Fig. 22.** Differential astrometry for common proper motion pairs shown in the sense primary minus secondary component. *Top:* Differences between parallaxes (mas, running medians over 3000 sources) before (blue) and after (magenta) zero point correction, as a function of the primary magnitude,  $10 < G < 15$  mag. *Middle:* Primary minus secondary parallaxes before and after zero point correction for stars brighter than  $G = 10$  mag (running medians over 100 sources). *Bottom:* Differential proper motion ( $\text{mas yr}^{-1}$ ) in right ascension (blue) and declination (orange) versus magnitude, running medians over 3000 sources.

allax, which should not, in general, be interpreted as a colour effect. On average, the correlation is, for example, positive near the Galactic centre and negative in the LMC, giving a very large peak-to-peak amplitude of  $0.2$  mas (Fig. 23, middle panel); although it is twice as small as for DR2 (Arenou et al. 2018, Fig. 18). After the Lindegren et al. (2020a) correction of the zero point, the variations were considerably reduced (Fig. 23, bottom panel).

### 3.10. Proper motions from star cluster analysis

For each star, we derived the differences of the proper motions  $\mu_{\alpha^*}$ ,  $\mu_\delta$  to the cluster median. This provides information about the zero point variations and about the uncertainties. Figures 25 and 24 present the results, which were scaled and not scaled to the nominal errors as function of  $G$ ,  $G_{\text{BP}} - G_{\text{RP}}$ , and in the colour-magnitude diagram. As already found for the parallaxes, a complex dependence of the difference with magnitude and colour

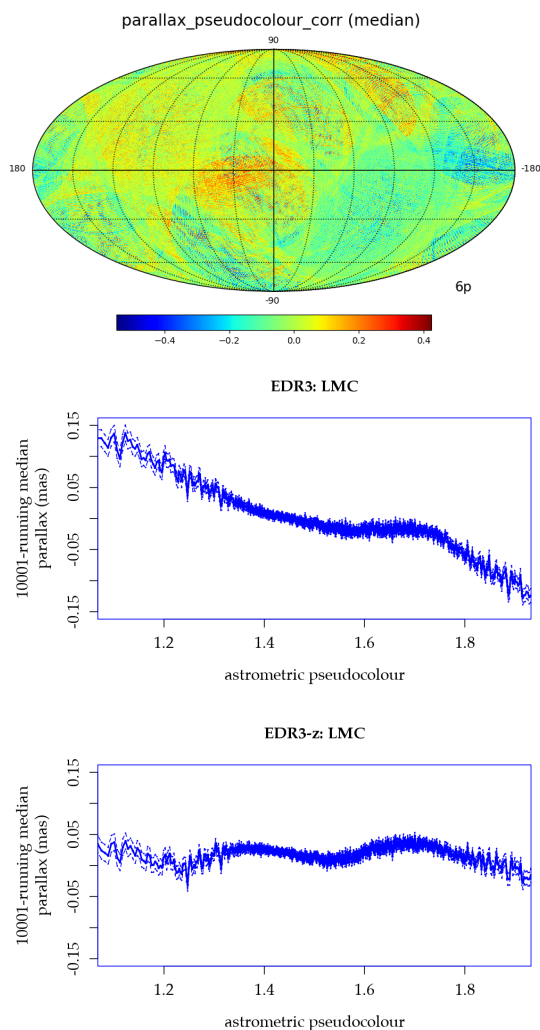


**Fig. 23.** *Top:* Correlation between parallax and pseudo-colour. *Middle:* Running median with uncertainty for LMC parallaxes where the negative correlation translates into systematics for the bluest and reddest sources. *Bottom:* LMC parallaxes after zero point correction.

is clearly visible. This reflects a variation in the zero point. In particular, a shift is present at  $G \sim 13$  mag in  $\mu_{\alpha^*}$ . When this difference is normalised to the nominal uncertainties, we find that these patterns are still present for brighter stars. This means that nominal uncertainties are underestimated in this magnitude and colour range. This effect is more evident in  $\mu_{\alpha^*}$ . Residuals are also present for very red stars ( $G_{BP} - G_{RP} \sim 1.5 - 2$  mag), where the results are less significant, since the statistics is relatively poor. This region can be contaminated by field stars.

We calculated the proper motion differences (median,  $\mu_{\alpha^*EDR3} - \mu_{\alpha^*DR2}$ ) for the whole cluster sample in *Gaia* DR2 and *Gaia* EDR3. The zero point median difference is  $-0.006 \text{ mas yr}^{-1}$  with a third quartile of  $0.06 \text{ mas yr}^{-1}$  in right ascension and in declination.

### 3.11. Proper motion precision in crowded areas

We compared the proper motions in the centre of M4 with external HST data (Nascimbeni et al. 2014), where high-quality relative proper motions are available. The precision of HST proper motions is of the order of  $0.33 \text{ mas yr}^{-1}$ . The ob-

served field is affected by crowding. We used the flux excess parameter  $C = (\text{phot\_bp\_mean\_flux} + \text{phot\_rp\_mean\_flux}) / \text{phot\_g\_mean\_flux}$ ,<sup>10</sup> as a tracer of crowding contamination. In Fig. 26, we present the *Gaia* proper motions distribution, the differences between *Gaia* and HST proper motions, and the scaled dispersion for the stars having *Gaia* nominal proper motion uncertainties  $< 0.2 \text{ mas yr}^{-1}$  and a moderate flux excess,  $C < 2$ . The scaled dispersion is very close to one for both  $\mu_{\alpha^*}$  and  $\mu_{\delta}$ , indicating that the nominal uncertainties were estimated correctly. Stars in this sample are not affected by crowding. Stars with a high level of contamination ( $C > 5$ ) are, on average, at 1.6-1.8 error bars from the expected value, that is to say *Gaia* nominal uncertainties on proper motions are underestimated for faint and/or contaminated stars. In any case, this represents a substantial improvement over *Gaia* DR2, where the nominal uncertainties were underestimated by a factor from two to three.

### 3.12. Goodness of fit for very bright stars

Although it is known that calibration errors or stellar duplicity may frequently make the quality of the astrometric solutions decrease, it may appear surprising to complain about a solution quality that is too good. Figure 27 (right panel) shows that the *ruwe* of sources brighter than 17 mag is near the expected value of one on average. However, it is smaller than one near the Galactic centre, and twice as small for stars brighter than  $G = 11$  mag (Fig. 27, left panel). The interpretation is the following: In this region, because most of the sources suffer from crowding, most sources should have some excess noise and not just a small fraction of them, as in other regions. Consequently, the attitude excess noise may have absorbed this source excess noise, leading to source solutions that appear much better than they truly are in reality. Consequently, the caveat is that the *ruwe* of bright sources in large crowded areas, and thus their *astrometric\_gof\_al*<sup>11</sup> too, may be much smaller than they should be.

## 4. Photometric quality of *Gaia* EDR3

The photometry in *Gaia* EDR3 consists of three broad bands: a  $G$  magnitude for (almost) all sources (1.8 billion) and a  $G_{BP}$  and  $G_{RP}$  for the large majority (1.5 billion). The photometry and its main validation is described in Riello et al. (2020), and here we present some additional validation. These tests include internal comparisons, comparisons with external catalogues, and some simulations.

Among the issues described by Riello et al. (2020), there are two issues for the user to be aware of. The first concerns sources where a reliable colour was not known at the beginning of the *Gaia* EDR3 processing and which therefore have not benefited from an optimal processing. These are all the 6p sources and many 2p sources, but none of the 5p sources. Riello et al. (2020) propose a correction to the catalogue  $G$  magnitude of the 6p sources that is typically of the order of a hundredth of a magnitude. For 2p sources, it is unfortunately not possible to know with certainty if a correction is needed. The second issue concerns the faintest  $G_{BP}$  sources, where a source with practically no signal, for example the  $G_{BP}$  flux for a faint, red source, will still have a significant flux assigned. This issue, which also ap-

<sup>10</sup> In the *Gaia* EDR3 archive, this is `phot_bp_rp_excess_factor`.

<sup>11</sup> `astrometric_gof_al` is the goodness of fit of the astrometric solution.



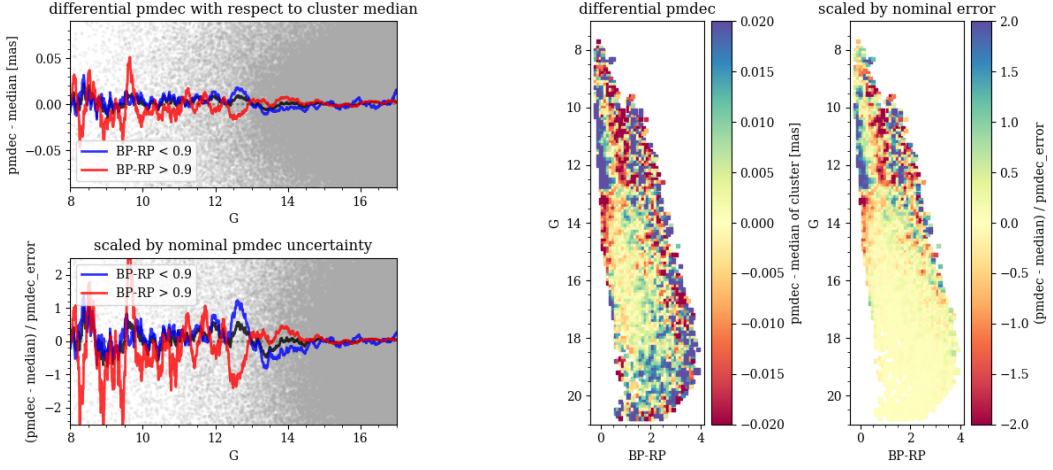


**Fig. 24.** *Left:* Difference between proper motions in declination and median value (top) and scaled (bottom) to the nominal uncertainties as a function of  $G$  for the whole cluster sample. The solid lines indicate the LOWESS of the sample; blue corresponds to stars bluer than  $G_{\text{BP}} - G_{\text{RP}} = 0.9$  mag and red is for objects redder than this limit. *Right:* Colour-magnitude diagram of the whole cluster sample where the colour indicates the difference between the star  $\mu_\delta$  and the cluster median. The rightmost panel is analogous to the left-hand panel, where the difference is scaled to the nominal uncertainties.

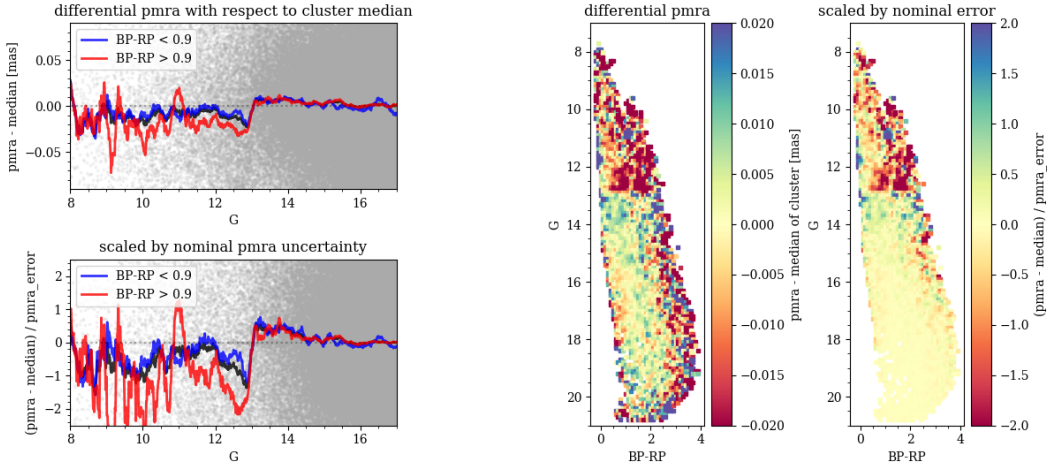


**Fig. 25.** Same as Fig.24, but for  $\mu_{\alpha^*}$ .

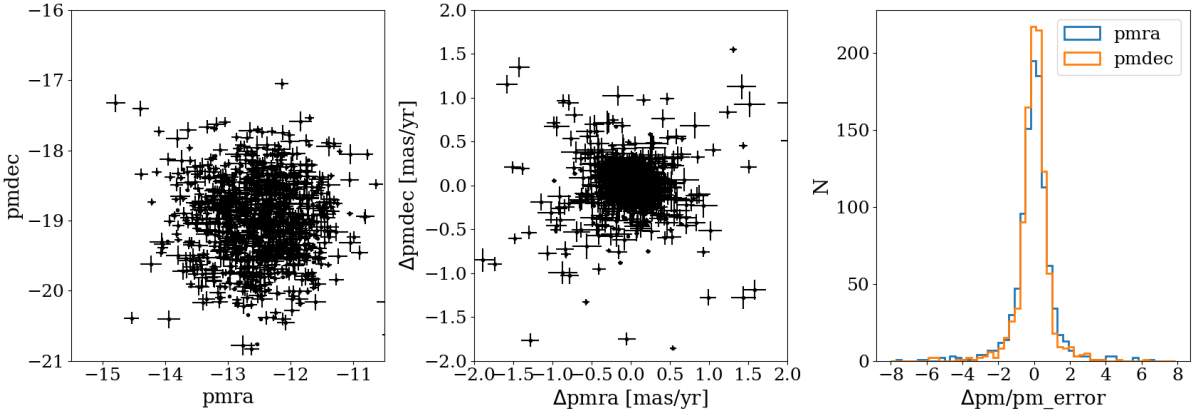


**Fig. 26.** *Left:* Gaia proper motion distribution in M4. Only stars with a proper motion error  $< 0.2 \text{ mas yr}^{-1}$  and flux excess parameter  $C < 2$  are plotted. *Centre:* Differences between proper motions in Gaia and in HST data. *Right:* Scaled dispersion for the stars having Gaia proper motions errors  $< 0.2 \text{ mas yr}^{-1}$  and flux excess parameter  $C < 2$ .

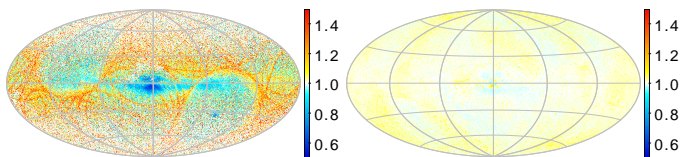


**Fig. 27.** Re-normalised unit-weight error for the astrometric solution,  $ruwe$ , for sources brighter than  $G = 11$  (left) and brighter than  $G = 17$  (right).

plies to a small population of  $G_{RP}$  fluxes, is discussed below in Sect. 4.2.

#### 4.1. Spurious photometric solutions

There were many unrealistically faint sources, down to  $G \sim 25.6$  mag, in a pre-release version of the catalogue. Such faint magnitudes can only arise from processing problems. After investigations in the photometric pipeline, PhotPipe, the root cause was traced to the way poor input spectral shape coefficients (SSCs) disturb the application of the photometric calibration (see Riello et al. 2020, sect. 4.4, eqs. 1–3). From the BP spectrum, four coefficients were derived:  $bp\_ssc0, \dots, bp\_ssc3$ , and four similar from RP. Quotients, such as  $bp\_ssc0/(bp\_ssc1+bp\_ssc2)$ , are used in the calibration model without taking into account that the denominator in certain cases may become extremely small and the quotient therefore extremely large. This is illustrated in Fig. 28, where we can see that in the majority of cases (in fact 82% for this sample of very faint sources) the principal blue and red quotients have reasonable values (lower left), and that these values are well separated from cases of very large values. This has allowed us to establish well defined thresholds, and the photometry of the sources with quotients larger than those thresholds is not published in the main catalogue because it is considered unreliable. The 5.4 million sources affected were reprocessed by PhotPipe using default SSCs, and the  $G$  flux derived this way is published in a separate file accessible in the *Gaia* EDR3 known issues<sup>12</sup> page.

Colours in *Gaia* DR2 were shown to be too blue for faint red sources and this also happens in *Gaia* EDR3. The  $phot\_bp\_rp\_excess\_factor$  parameter gives a measure of the coherence among  $G$ ,  $G_{BP}$ , and  $G_{RP}$  and can be used to identify the problematic cases. For those cases, the use of the colour  $G - G_{RP}$  instead of  $G_{BP} - G_{RP}$  may be more useful. Riello et al. (2020) identify the root cause of the problem to be a flux threshold applied to the individual transits when computing the mean photometry. We explore this question below.

#### 4.2. Transit-level flux threshold

The  $G_{BP}$  and  $G_{RP}$  mean fluxes were derived from the epoch fluxes at the several transits of a source across the focal plane during the mission. As discussed by Riello et al. (2020) (sect. 8.1), in the computation of the mean fluxes, a threshold of  $1 e^- s^{-1}$  was introduced for the individual transits. Transits with fluxes below that threshold were excluded from the computation of the mean fluxes. This introduces a bias in the mean fluxes for the faintest sources, as the distribution of noise-affected epoch fluxes becomes truncated when the flux of a source becomes so

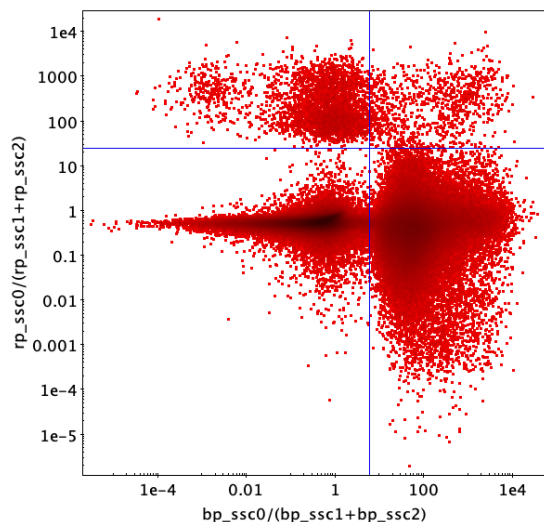


**Fig. 28.** Quotients of blue and red spectral shape coefficients for the set of sources fainter than  $G \sim 21.7$  mag. The photometry for sources with quotients larger than the thresholds (blue lines) were filtered for the publication (see text).

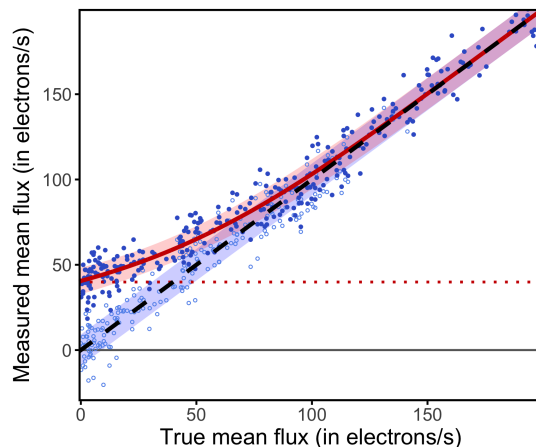


**Fig. 29.** Simulated mean fluxes as a function of the true mean flux in the presence of the  $1 e^- s^{-1}$  threshold (dark filled symbols) and without (light open symbols). The mean and the  $1\sigma$  confidence intervals are shown as lines and shaded regions. The dotted line indicates the lower bound of the mean in the presence of the threshold.

low that the distribution of epoch fluxes reaches the threshold. To illustrate the effect, we simulated mean fluxes by applying and not applying the threshold, under the simplifying assumption of the same normally distributed background noise of  $50 e^- s^{-1}$  and 30 transits. As background noise, we subsume here all noise contributions other than the source’s photon noise, that is to say contributions from detector and electronics effects, the sky background, and stray light. In reality, this background noise can vary significantly between different transits. Simulations of measured mean fluxes for sources by applying and not applying the threshold as a function of true source flux is shown in Fig. 29, together with the means, and the  $1\sigma$  confidence intervals. As the source fluxes become low, the measured mean fluxes systematically deviate from the true fluxes, and the mean of the distributions of mean fluxes meet a lower bound. For a threshold much smaller

<sup>12</sup> <https://www.cosmos.esa.int/web/gaia/edr3-known-issues>

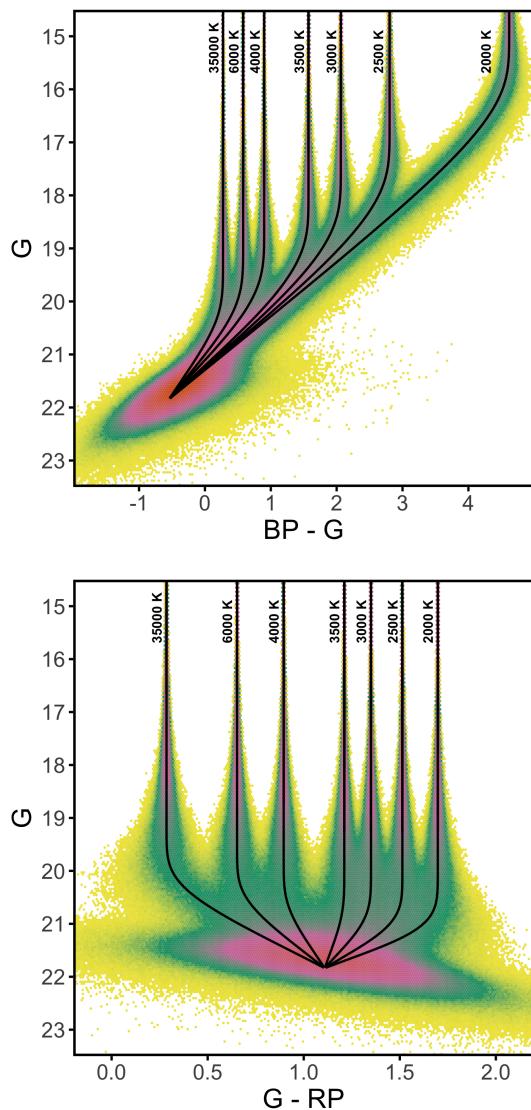


**Fig. 30.** Distribution of 5 million simulated mean magnitudes for BaSeL spectra with effective temperatures from 2000 K to 35000 K, in the presence of a  $1 e^{-} s^{-1}$  threshold, in the  $G_{BP} - G$  versus  $G$  (upper panel) and the  $G - G_{RP}$  versus  $G$  (lower panel) colour-magnitude diagrams. The solid lines indicate the mean.

than the background noise level, this lower bound on the mean is approximately 0.8 times the standard deviation of the background noise.

Sources are detected based on an estimate of their  $G$  band magnitude, with a detection limit well above the  $1 e^{-} s^{-1}$  threshold. Also since astronomical sources do not become arbitrarily blue, the flux of detected sources measured in the  $G_{RP}$  passband cannot become arbitrarily smaller than the flux in the  $G$  band. But as astronomical sources can become arbitrarily red, the flux in the  $G_{BP}$  passband can become smaller than the  $G$  band flux without bound. Sufficiently red sources can therefore have  $G_{BP}$  fluxes that even fall below the detection limit while having significant fluxes in the  $G$  and  $G_{RP}$  passbands. As a consequence, the bias on the mean flux for faint sources resulting from the threshold mostly affects the  $G_{BP}$  fluxes, and it only has a much smaller effect for the  $G_{RP}$  fluxes.

As a consequence of the  $G_{BP}$  fluxes being far more biased towards larger values than the  $G$  and  $G_{RP}$  fluxes for faint sources, a 'turn' in the colour-magnitude diagram involving  $G_{BP}$  magnitudes results for faint sources, as shown by Riello et al. (2020). To illustrate the effect further, we simulated BaSeL spectra (Lejeune et al. 1997) with different effective temperatures (for solar metallicity and a surface gravity,  $\log g$ , of four) in the  $G$  versus  $G_{BP} - G$  and  $G - G_{RP}$  colour-magnitude diagrams. The distribution of the simulated mean magnitudes, together with the mean of the distributions as a function of colour, is shown in Fig. 30. For the  $G$  versus  $G_{BP} - G$  colour-magnitude diagram, the strong turn in the distributions is visible, which starts at brighter  $G$  magnitudes as the source becomes cooler, and thus redder. If the fluxes approach the noise level, the distributions become independent of the spectral energy distributions of the sources, and the means of the distributions for all sources converge at the same location in the colour-magnitude diagram. For thresholds much smaller than the noise level, the position of this convergence point only depends on the background noise and, when converting fluxes into magnitudes, on the zero points of the passbands.

For the  $G$  versus  $G - G_{RP}$  colour-magnitude diagram, the effect of convergence on the same mean position in the diagram for faint sources is also present. However, the turning of the distributions occurs at fainter magnitudes, and the effect for blue sources is much smaller than for the red sources in the  $G$  versus  $G_{BP} - G$  case.

To minimise the effects introduced by the threshold on the interpretation of photometric data, it is thus advisable to avoid the use of  $G_{BP}$  magnitudes fainter than about 20.5, corresponding to  $G_{BP}$  fluxes below approximately  $86 e^{-} s^{-1}$ , if possible. For  $G_{RP}$  magnitudes, significant bias effects occur at values fainter than about 20.0, corresponding to  $G_{RP}$  fluxes below approximately  $79 e^{-} s^{-1}$ . Since the bias effects are strongest in  $G_{BP}$ , the  $G - G_{RP}$  colour is more reliable than colours involving  $G_{BP}$ .

#### 4.3. Photometry of the 6p solutions

We tested the correction to the  $G$  magnitude proposed by Riello et al. (2020) for stars with 6p solutions, that is with a default colour in the image parameter determination (IPD), on the red clump sample of APOGEE DR16 (Bovy et al. 2014). The variation in the colour-colour relation for those red clump stars is due to the variation in the extinction and it is curved due to the non-linearity of the extinction coefficient with extinction. In the top panel of Fig. 31, there are two effects that can be seen. The first one is that of the transit-level flux threshold, discussed in the previous section, seen as a plume of stars becoming bluer than the global relation. The second effect is the difference between the colour-colour curves of the 5p and 6p solutions (black and red, respectively). If we were to add the  $G$  magnitude correction as proposed by Riello et al. (2020, sect. 8.3) and remove those sources with  $G_{BP} > 20.5$  mag as proposed in the previous section, we would recover the expected colour-colour relation.

#### 4.4. Photometric accuracy

The systematic errors of the photometry can be studied in both internal and external comparisons as well as from galaxy models of the Milky Way. In addition, we look at the changes with respect to *Gaia* DR2.



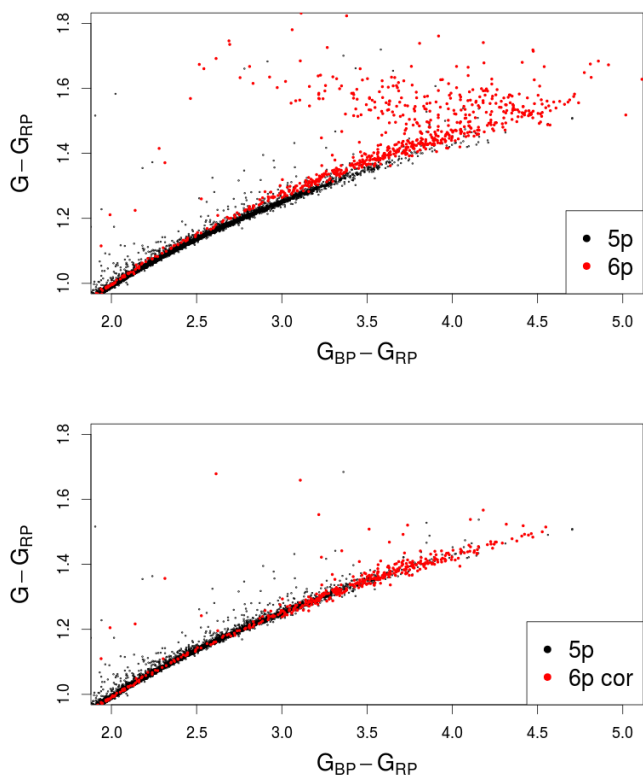


**Fig. 31.** Colour-colour relation of the APOGEE DR16 red clump sample. Stars with 5p astrometric solutions are shown with black dots, and the ones with 6p solutions are shown with red dots. *Top*: The full sample. *Bottom*: After removing stars with  $G_{BP} > 20.5$  mag and correcting the  $G$  photometry of the 6p solutions using the recipe of Riello et al. (2020).

#### 4.4.1. Internal comparisons

We studied the internal trends as a function of magnitude. Figure 32 (top panel) shows the residuals from the median  $G - G_{RP} = f(G_{BP} - G_{RP})$  relation as a function of  $G$  on a sample of stars in the upper part of the H-R diagram with low extinction, that is  $A_0 < 0.05$  mag according to the 3D extinction map of Lallement et al. (2019) and  $M_G < 4$  mag,<sup>13</sup> taking into account the parallax error at 2 sigma. We further selected only stars with relative photometric errors better than 2% in  $G$  and 5% in  $G_{BP}$  and  $G_{RP}$ . These strict criteria lead to a well behaved colour-colour relation but to less than 800 000 stars, which are mostly close by and therefore relatively bright. There is a small trend with magnitude which is much smaller than in *Gaia* DR2 (Arenou et al. 2018). Discontinuities at  $G \sim 10.8$  and 13 mag of only about 0.5 and 1 mmag are also much smaller than in *Gaia* DR2. Figure 32 (bottom panel) shows that for blue stars, the trend with magnitude is still stronger (see also sect. 8.4 of Riello et al. (2020)), but the amplitude is about three times smaller than in *Gaia* DR2 (Arenou et al. 2018, fig. 35).

Figure 33 shows the median  $G_{BP} - G_{RP}$  colours in a dense field in the case of *Gaia* DR2 and *Gaia* EDR3. One can appreciate that the artefacts from the scan patterns have decreased quite a bit.

<sup>13</sup>  $\text{parallax} + 2 \times \text{parallax\_error} < \exp((4 - \text{phot\_g\_mean\_mag} + 10) \times 0.46)$

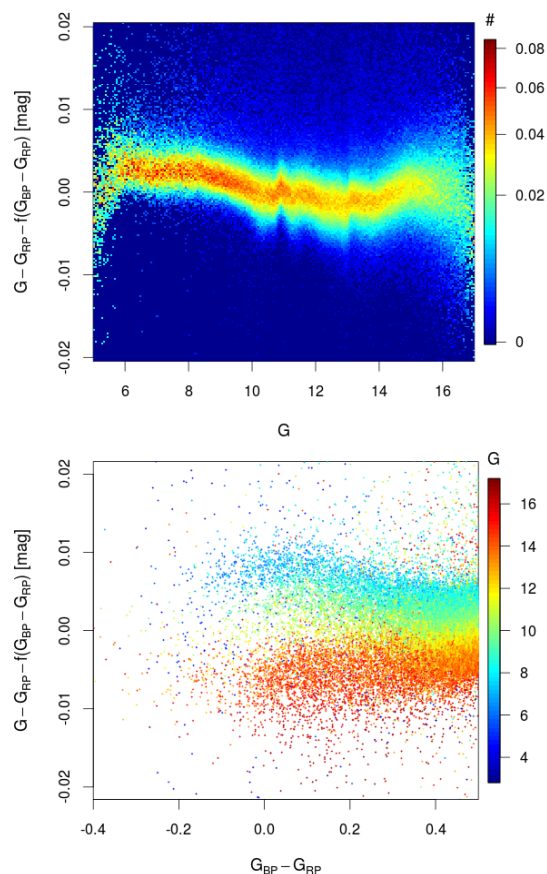


**Fig. 32.** Residuals from a global  $G - G_{RP} = f(G_{BP} - G_{RP})$  relation for a sample of luminous, low extinction stars ( $A_0 < 0.05$  mag,  $M_G < 4$  mag). *Top*: As a function of  $G$ , colour-coded by the number of stars normalised by the total number of stars per magnitude bin. *Bottom*: As a function of  $G_{BP} - G_{RP}$  for a sample of bluer stars, colour-coded by the magnitude.

#### 4.4.2. Comparisons with external catalogues

We compared *Gaia* EDR3 photometry to the HIPPARCOS, Tycho-2, Landolt standards (Landolt 1983, 1992, 2007, 2009, 2013; Clem & Landolt 2013, 2016), the SDSS tertiary standard stars of Betoule et al. (2013), and Pan-STARRS1 (PS1, Chambers et al. 2016) photometry. For HIPPARCOS, Tycho-2, we selected low extinction stars ( $A_0 < 0.05$  mag) using the 3D extinction map of Lallement et al. (2019) and taking into account the parallax uncertainty. For SDSS and PS1, we selected stars with a high galactic latitude. For the Landolt catalogue, we selected both on  $|b| > 30^\circ$  and  $A_0 < 0.05$  mag for low latitude stars. We selected only stars with  $\text{flux\_over\_error} > 20$ , corresponding to photometric errors of  $< 0.05$  mag for the external catalogues, to ensure we were working with roughly Gaussian errors in magnitude space. An empirical robust spline regression was derived which models the global colour-colour relation. The residuals from those models are plotted as a function of magnitude in Fig. 34. We also added in Fig. 34 the comparison with the magnitude computed on the CALSPEC (Bohlin et al. 2014, 2020 April Update) spectra combined with the *Gaia* EDR3 instrument response. The global zero point offset observed is smaller than 1%, which is in agreement with the CALSPEC expected accuracy (Bohlin et al. 2014) and our observation of the variations between different CALSPEC releases.

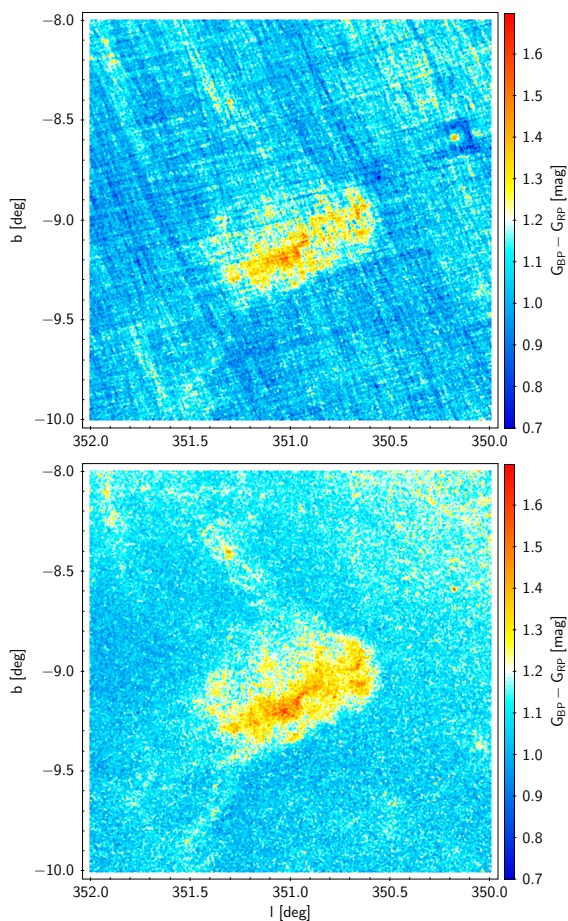


**Fig. 33.** Median colours  $G_{BP} - G_{RP}$  in a dense field (Galactic coordinates) showing artefacts from the scan pattern in *Gaia* DR2 (top), which have almost disappeared in *Gaia* EDR3 (bottom).

Figure 34 shows that the strong saturation effect present in *Gaia* DR2 as well as the variation of the  $G$  zero point with magnitude have been removed in *Gaia* EDR3. Variations are now smaller than 0.04 mag. The trend as a function of magnitude for bright stars are consistent between the HIPPARCOS, Tycho-2, and CALSPEC results. On the faint end, a global increase in the residuals is observed in  $G_{RP}$  consistently between Landolt, Panstarrs, and SDSS, while for  $G_{BP}$  those three surveys do not give a consistent amplitude of the variation. We recall that applying our procedure to colour-colour relations within the external catalogues’ photometric bands leads to global variations of the order of 2 mmag/mag for PS1 and larger for SDSS (Arenou et al. 2018).

#### 4.4.3. Global comparison of $G$ to *Gaia* DR2

Figure 35 shows the full sky mean difference of the  $G$  magnitudes between *Gaia* EDR3 and *Gaia* DR2. Although the comparison between both releases is not straightforward because their photometric systems are slightly different, as discussed in Riello et al. (2020), the map does illustrate specific areas where the differences are large, though it is generally at the level of a couple of hundredths of a magnitude. As in the case of astrometry, we expect that the map mainly shows the errors of *Gaia* DR2 and hence the improvements reached in *Gaia* EDR3.

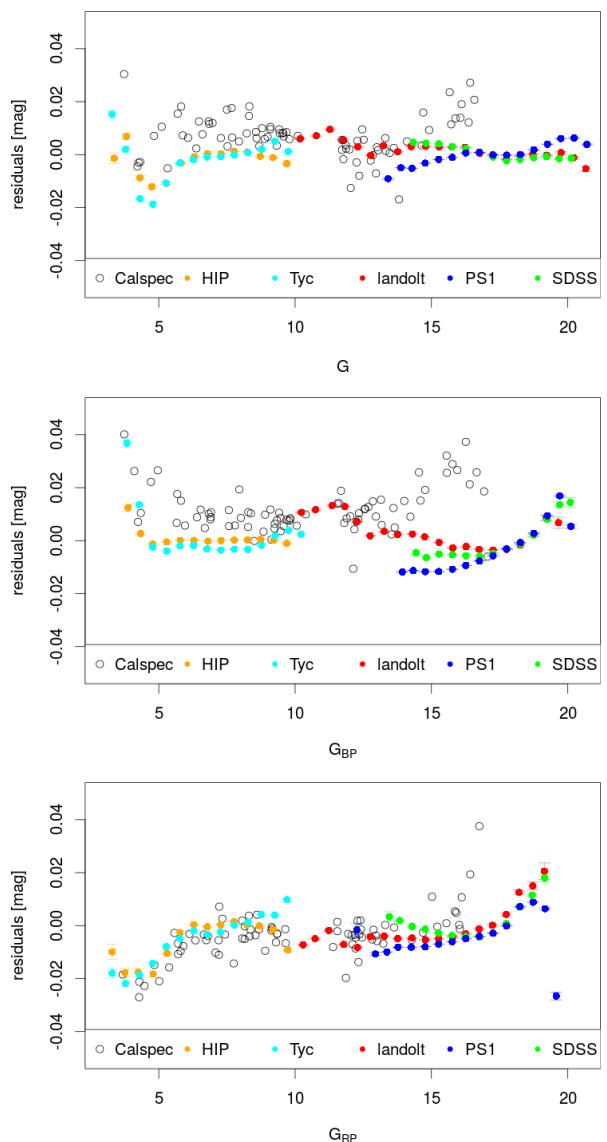


**Fig. 34.** From top to bottom,  $G$ ,  $G_{BP}$ , and  $G_{RP}$  photometry (hereafter referred to as  $X$ ) versus external photometry: CALSPEC (black dots) corresponding to  $X - X(\text{calspec})$ ; HIPPARCOS (orange) residuals of the global  $X - H_p = f(V - I)$  spline; Tycho-2 (cyan) residuals of the global  $X - V_T = f(B_T - V_T)$  spline; Landolt (red) residuals of the global  $X - V = f(V - I)$  spline; and PS1 (blue) and SDSS (green) residuals of the global  $X - r = f(g - i)$  spline for SDSS and PS1. The zero point of those different residuals is arbitrary with the exception of the CALSPEC results.

#### 4.4.4. Comparisons of $G_{BP} - G_{RP}$ colours to a Milky Way model

The median of the  $G_{BP} - G_{RP}$  colour is computed in each healpix bin of the sky map, for *Gaia* EDR3 data and GOG20 simulations. At intermediate and faint magnitudes, the differences can be large in the Galactic plane and are clearly linked to the extinction. At higher latitudes, the model is in agreement with the data at the level of 0.1 mag. However at bright magnitudes ( $G < 9$  mag at intermediate latitudes and upwards,  $G < 12$  mag in the plane), the data deviate from the values predicted by the model, from  $-0.2$  mag to more than  $-1$  mag at  $G = 5$ . This discrepancy is slightly reduced compared to *Gaia* DR2. This could be a possible problem in the colour determination for those

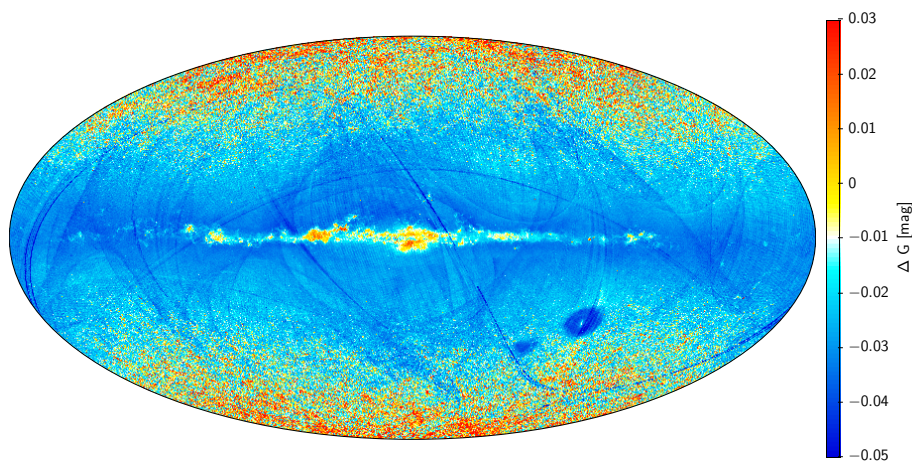


**Fig. 35.** Map in Galactic coordinates of the mean difference of the  $G$  magnitudes between *Gaia* EDR3 and *Gaia* DR2.

bright stars. However, since we are comparing the median value in healpix bins, an underestimate of blue bright stars in the model could rather explain this remaining difference, in particular in the brightest bins affected by large Poisson noise.

#### 4.5. Photometric precision

##### 4.5.1. Internal comparisons

A comparison between mean  $G$  magnitudes provided in the *Gaia* DR2 and *Gaia* EDR3 catalogues for a sample of 140 635 sources classified as RR Lyrae variables in *Gaia* DR2, for which both estimates of the mean  $G$  magnitude are available, shows that there is a difference in magnitudes of more than 0.5 mag for 2044 sources, with the *Gaia* EDR3 magnitudes being fainter. The *Gaia* EDR3  $G$  magnitudes plotted versus the *Gaia* DR2  $G$  magnitudes for 140 635 RR Lyrae stars are shown in Fig. 36, where sources which have a difference in magnitude more and less than 0.5 mag are marked with red and black points, respectively. The figure shows that there is good agreement for a majority of stars, while for 2044 sources shown with red points there is a systematic shift in magnitudes, with the *Gaia* EDR3 magnitudes being fainter. Among these 2044 sources, 908 are listed by Clementini et al. (2019) in their Table C1 as known galaxies misclassified as RR Lyrae variables in *Gaia* DR2. Furthermore, a more detailed analysis of the 2044 stars performed with a dedicated pipeline shows that the vast majority of these sources are extended objects. The fainter magnitudes for these 2044 sources are, therefore, most likely due to an improved background determination in the *Gaia* EDR3 processing.

#### 4.6. Photometric quality indicators

*Gaia* EDR3 includes the flux excess factor, `phot_bp_rp_excess_factor`<sup>14</sup> as an indicator of the coherence among  $G$ ,  $G_{BP}$ , and  $G_{RP}$  fluxes. It is sensitive to contamination by close-by sources in dense fields, binarity, background subtraction problems, as well as extended objects. The improvement of the full pipe-line calibrations in *Gaia* EDR3 yields a decrease in the excess factor with respect to *Gaia* DR2 as it can be seen in Fig. 37. The fainter the magnitude is, the larger the improvement, which is more noticeable for point-like sources with  $G > 19$  mag. Sources

<sup>14</sup> Riello et al. (2020) define a corrected factor  $C^*$  that takes the dependence of the `phot_bp_rp_excess_factor` with  $G_{BP} - G_{RP}$  colour into account.

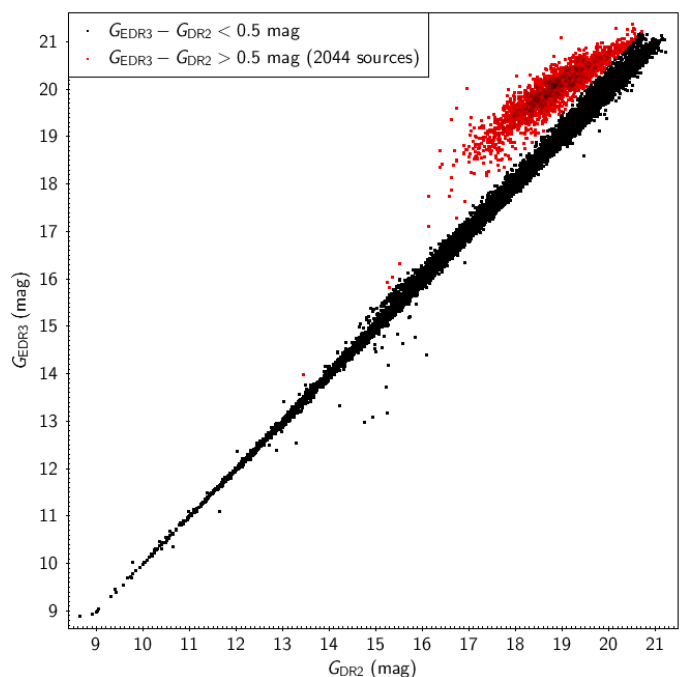


**Fig. 36.** Comparison between mean  $G$  magnitudes provided in the *Gaia* DR2 and *Gaia* EDR3 catalogues for 140 635 RR Lyrae variables. Black and red points show sources with a difference in magnitudes of less and more than 0.5 mag, respectively.

with `phot_bp_rp_excess_factor > 5` were published in *Gaia* DR2 without  $G_{BP}$  and  $G_{RP}$  fluxes. In *Gaia* EDR3, this filter has not been applied and it is up to the users to decide on the use of the photometry in case of a large excess of flux. Small amplitude artefacts due to the scanning pattern still remain (bottom panel in Fig. 37). Criteria for filtering the incoherent fluxes are discussed in sect. 9.4 of (Riello et al. 2020).

#### 4.7. Photometry in crowded areas

Photometry in highly crowded areas is of lower quality than in non crowded regions. This is the case of all the globular clusters, where the photometry in the inner regions is shifted in colour and magnitude as an effect of crowding, with a large dispersion. This effect was visible in *Gaia* DR2 and it is still present in *Gaia* EDR3, in spite of the improvements in the number of observations and in the photometry. See for instance Fig. 38, show-



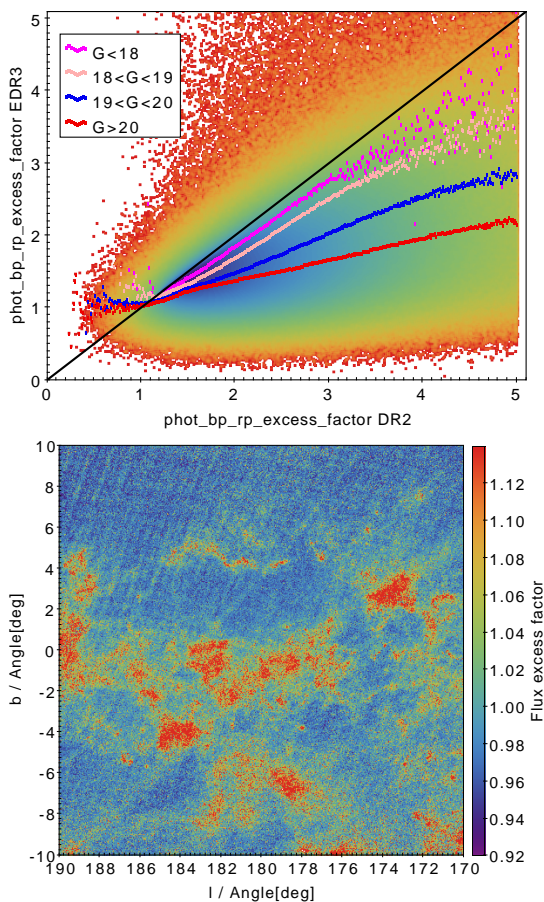


**Fig. 37.** *Top:* Excess flux for 36 million sources towards the direction  $l \in (10^\circ, 20^\circ)$  and the  $b \in (-5^\circ, 5^\circ)$  direction. The black line is the identity and the other ones are the median for different ranges of  $G$ . *Bottom:* Excess flux for 14 million sources towards the anti-centre direction. The colour code accounts for the ratio between the  $\log_{10}$  `phot_bp_rp_excess_factor` and the relation  $0.05 + 0.039(G_{BP} - G_{RP})$ , which is the approximate locus of well behaved stars.

ing the quality of the photometry in the inner and outer regions of NGC 5986.

#### 4.7.1. Comparison with HST photometry in crowded areas

We compare  $G$ ,  $G_{BP}$ , and  $G_{RP}$  photometry with the high quality HST ACS/F606W magnitudes in M4 using the data set from Bedin et al. (2013). The precision of the HST photometry is at the level of a few milli-mag. We subtracted the median difference between *Gaia* and HST photometry, and we calculated the variation of the residuals for stars having  $1.4 < G_{BP} - G_{RP} < 1.5$ . We selected a fix range to avoid colour effects. The residuals around the median value in  $G$  are of the order of 0.025-0.03 mag. These values are in agreement with the comparison with external catalogues presented in Sect. 4.4.2. However, a clear trend with the magnitude and with the flux excess is visible (see Fig. 39). We recall here that the flux excess can be considered as a proxy of the level of contamination due to neighbouring stars. The detected trend is an effect of the crowding, showing that faint stars located in regions with high contamination present larger residuals. No trend is present in  $G_{BP}$  and  $G_{RP}$ , albeit with a large dispersion due to the high level of contamination.

## 5. Global validation of *Gaia* EDR3

Here, we perform a global comparison of the statistical properties of *Gaia* EDR3 to *Gaia* DR2. This complements the detailed analyses presented in the previous sections on the astrometry and the photometry. For the statistical comparison, we use the *Kullback–Liebler Divergence* (KLD) to establish the degree of correlations and clustering between observables or, more generally, entries in the catalogue. The KLD is defined as

$$KLD = - \int d^n x p(\mathbf{x}) \log[p(\mathbf{x})/q(\mathbf{x})], \quad (2)$$

where  $\mathbf{x}$  is the  $n$ -dimensional vector of the observables considered,  $p(\mathbf{x})$  is the distribution of these observables in the dataset, and  $q(\mathbf{x}) = \prod_i p_i(x_i)$ , that is to say the product of marginalised 1D distributions of each of the observables. Large values of the KLD indicate highly structured data, while low values of the KLD (below  $\sim 0.5$ ) correspond to little information content.

We compared the performance of *Gaia* EDR3 to *Gaia* DR2 in two ways: **1)** we considered all 2D subspaces ( $n = 2$ ), that is all possible combinations of pairs of observables in the catalogues (e.g.  $(G, \varpi)$ ,  $(\sigma_\varpi, \mu_\delta)$ , etc); and **2)** we computed the KLD for 3D subspaces ( $n = 3$ ) for small regions on the sky, with two of the three observables being  $\alpha$  and  $\delta$ . In both cases, we excluded outliers by considering 99% of the data for each observable (e.g. for the  $G$ -magnitude, the range used for *Gaia* EDR3 is 11.69 - 21.62).

Figure 40 shows the distribution of KLD values for the 2D comparison between *Gaia* EDR3 and *Gaia* DR2. While a few 2D subspaces lie very close to the 1:1 line, indicating a similar behaviour in *Gaia* EDR3 and *Gaia* DR2, there is a large set of subspaces for which the KLD has decreased in *Gaia* EDR3. Furthermore, these sets follow a parallel track to the 1:1 line, with an offset of about 0.17. These are mostly subspaces involving astrometric uncertainties. This decrease can be fully attributed to the smaller uncertainties since the KLD is the relative entropy  $\log[p(x)/q(x)]$  weighted by the distribution of  $p(x)$  values, which have become smaller in the case of the uncertainties. The subspaces with the largest decrease in the KLD for *Gaia* EDR3 are those including photometric uncertainties, as may be expected. On the other hand, a few subspaces depict an increase in the KLD, and these are mostly subspaces combining the number of observations or visibility periods. In this case, the range of the parameter has increased significantly from *Gaia* DR2 to *Gaia* EDR3.

We also computed the KLD in 3D in four circular patches on the sky, each with a radius of 5 deg, and centred on  $(l, b) = (-90^\circ, -45^\circ)$ ,  $(-90^\circ, 45^\circ)$ ,  $(90^\circ, -45^\circ)$ , and  $(90^\circ, 45^\circ)$ , respectively. As for *Gaia* DR2, patches that are symmetric with respect to the Galactic plane exhibit a similar behaviour. However, there is also a strong dependence on their location with respect to the scanning law. When compared with *Gaia* DR2, we find *Gaia* EDR3 to be systematically less clustered in subspaces containing astrometric or photometric information, for example (see e.g. Fig. 33). We interpret this as an improvement on the systematics introduced by the scanning law. Nonetheless, we still find some amount of residual clustering in the astrometric parameters which appear to be sensitive to the orientation of the visits, and not just the number of observations (as seen, for example, in Fig. 12).

The global analyses performed here thus confirm that the quality of *Gaia* EDR3 has improved significantly compared to that of *Gaia* DR2. The largest improvement is found for the photometry, since some ‘systematics’ associated to the imprint of the

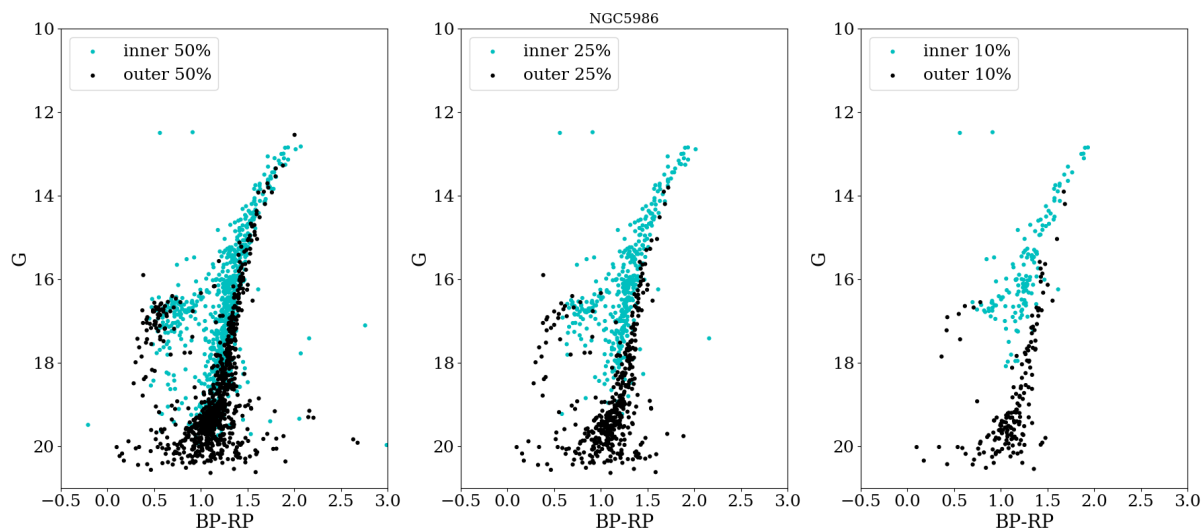


**Fig. 38.** Colour magnitude diagram in the inner (blue) and outer (black) regions of NGC 5986 in three different areas: inner 50% and outer 50% (left); inner 25% and outer 25% (centre); and inner 10% and outer 10% (right).

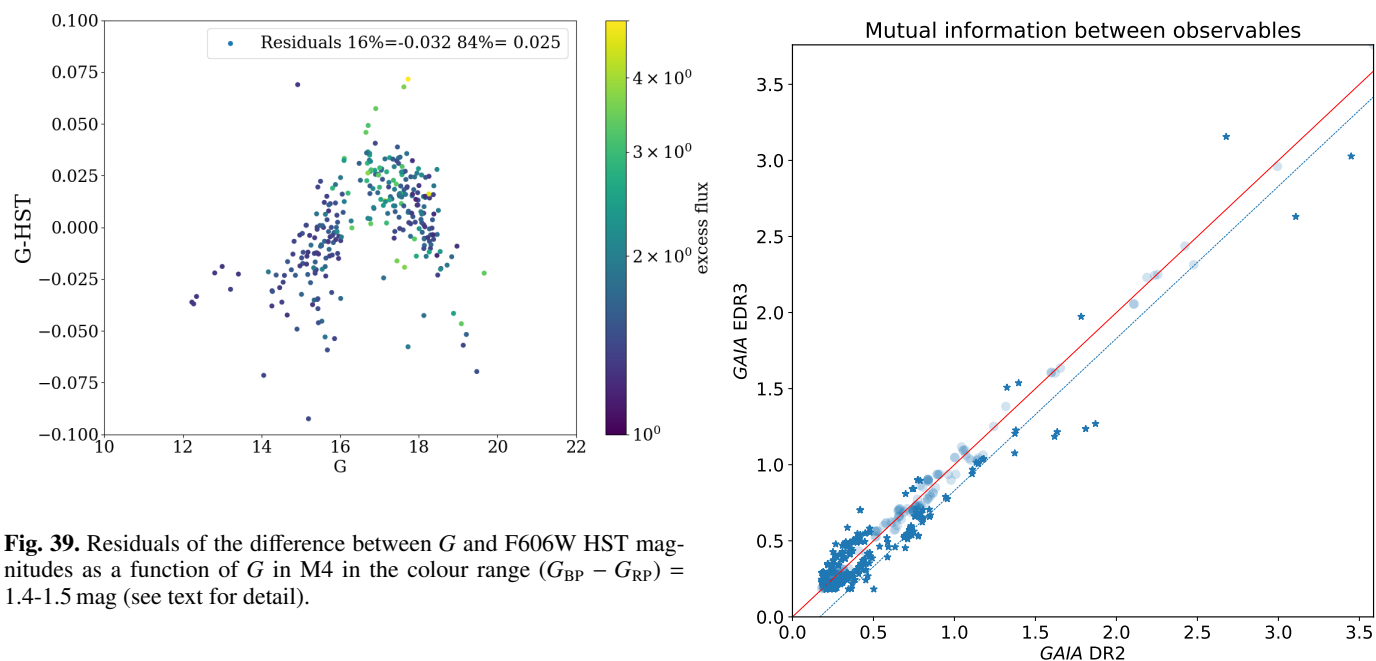


**Fig. 39.** Residuals of the difference between  $G$  and F606W HST magnitudes as a function of  $G$  in M4 in the colour range ( $G_{BP} - G_{RP}$ ) = 1.4-1.5 mag (see text for detail).

scanning law pattern are still present in the astrometric parameters and their uncertainties.

## 6. Conclusions and recommendations

*Gaia* EDR3 provides updated astrometry and photometry for 1 811 709 771 sources. Of these, 19.0% have a 2p astrometric solution, that is to say only a position, 32.3% have a 5p solution, that is also including the parallax and proper motion, and 48.7% have a 6p solution where also a colour parameter, the pseudo-colour, is determined. For the photometry, the catalogue gives  $G$  magnitudes for 99.7% of the sources,  $G_{BP}$  for 85.1%,  $G_{RP}$  for 85.8%, and a  $G_{BP} - G_{RP}$  colour for 85.0%.

In this paper, we have presented a series of tests aimed at illustrating the quality of the catalogue, with an emphasis on known issues as it is natural for a validation paper. The idea has been that these examples can serve as a guide for actual use cases. In many tests, we have used rather strict selection criteria

**Fig. 40.** Comparison of 2D KLD between *Gaia* EDR3 and *Gaia* DR2. The 1:1 line is shown in red, while subspaces for which KLD was deviated by at least 10% with respect to DR2 are shown as "\*", respectively. The blue dashed line is a guide to the low KLD sequence at an offset of about 0.17 from the 1:1 line.

in order to better answer certain questions, but selection criteria should always be chosen to fit the case at hand. For convenience, we summarise the principal recommendations from this validation exercise in Table 2. Additional advice and recommendations can be found in the astrometric and photometric processing papers (Lindegren et al. 2020b; Riello et al. 2020).

The catalogue is the third in a series, and it is natural to check where it stands compared to the previous release, *Gaia* DR2. In particular, we note the following.

- It contains 7% more sources.

**Table 2.** Principal recommendations for using *Gaia* EDR3.

Item	Recommendation	Reference
Find a DR2 source	Use dedicated neighbourhood table	Sect. 2.1
Isolated source?	For astrometry: check <code>ruwe</code> and image parameter statistics. For $G_{BP}$ and $G_{RP}$ : check statistics on blended and contaminated transits	Fig. 14, Table B.1
Parallax zero point	Consider applying the correction by Lindegren et al. (2020a)	Sect. 3
Spurious astrometry	Check – statistically – for the presence of spurious parallaxes and proper motions	Sect. 3.2
Missing $G$	Alternative $G$ photometry is available	Sect. 4.1
$G$ magnitude	A small correction should be added for 6p solutions	Sect. 4.3
$G_{BP}$ magnitude	Be aware of a strong bias for $G_{BP} > 20.5$ mag	Sect. 4.2
$G_{RP}$ magnitude	Be aware of a strong bias for $G_{RP} > 20$ mag	Sect. 4.2
Colour	Use $G - G_{RP}$ instead of $G_{BP} - G_{RP}$ when faint red sources are included	Sect. 4.2
$G$ , $G_{BP}$ , $G_{RP}$ coherence	Check the $C^*$ value defined by Riello et al. (2020)	Sect. 4.6

- It presents parallaxes and proper motions for 10% more sources.
- It has a high completeness until  $G \sim 19$  mag, cf. Sect. 2.2.
- The completeness has improved in dense areas, cf. Sect. 2.4.
- The angular resolution has improved but is still dropping fast below  $0''.7$ , cf. Sect. 2.3.
- Source identifiers from *Gaia* DR2 have, in general, been maintained for 97% of the sources, cf. Sect. 2.1, but it is not advisable to rely on the identifier alone. If the counterpart of a *Gaia* DR2 source is sought, we recommend using the table `gaiaedr3.dr2_neighbourhood` instead, which is available in the *Gaia* archive.
- A little more than half a percent of *Gaia* DR2 sources are not found in *Gaia* EDR3 within 50 mas, cf. Sect. 2.1. They are mostly faint and some are likely to be spurious sources.
- The catalogue contains several fields that help to identify sources with a close neighbour. In addition to the parameters detailing the internal consistencies of the astrometric and photometric solutions already in *Gaia* DR2, the catalogue now also provides statistics on the images themselves, such as `ipd_frac_multi_peak`, `ipd_harmonic_gof_amplitude`, etc., cf. Table B.1.
- For a guide to the full list of parameters, we recommend the datamodel description in the online documentation.<sup>15</sup>

For the astrometry, the precision has significantly benefited from the additional year of observations. In addition, we notice the following.

- There are fewer sources than in *Gaia* DR2 with incomplete astrometry (2p), for example 1.5% as compared to 2.4% for  $G < 19$  mag, which is mainly due to the increase in number of observations, cf. Sect. 2.6.

- A significant number of 2p solutions, more than half for  $G < 19$  mag, are caused by the insufficiency of a 5p or 6p source model, cf. Sect. 2.6.
- In specific sky areas, there can be mean differences in position with respect to *Gaia* DR2 at the 1 mas level.
- The systematic errors in parallax – as shown by QSOs – are significantly smaller than in *Gaia* DR2, cf. Sect. 3.3. They can be further diminished by applying the corrections detailed in Lindegren et al. (2020a), and we recommend following the guidelines from that paper.
- High proper motion sources now have a much improved reliability with no negative parallaxes for sources with motions above  $300 \text{ mas yr}^{-1}$ , cf. Sect. 2.5.
- We have 1.6% spurious solutions among sources with  $\varpi/\sigma_\varpi > 5$ , cf. Sect. 3.2, but this fraction is much less for brighter sources and for 5p solutions. We recommend testing any specific sample, designed to contain only positive parallaxes, by also selecting the corresponding sample with negative parallaxes.
- Parallax uncertainties are underestimated, but less than for *Gaia* DR2, cf. Sect. 3.7.
- Parallaxes have up to a +0.02 mas level offset in zero point for sources brighter than  $G = 13$  mag as shown in binaries and in clusters. It is mostly removed when applying the Lindegren et al. (2020a) parallax correction.
- Parallaxes for 6p solutions show a clear correlation with the pseudo-colour in the LMC, which is largely removed with the Lindegren et al. (2020a) correction.
- Proper motions in right ascension have a small offset of  $0.01 \text{ mas yr}^{-1}$  for sources brighter than  $G = 13$  mag, cf. Figs. 22 and 25. This is seen in proper motion pairs as well as in clusters.
- The quality indicators `ruwe` and `astrometric_gof_al` are strongly underestimated for bright sources in crowded areas, cf. Sect. 3.12.

For the photometry, nearly all issues found with *Gaia* DR2 (Arenou et al. 2018) are either solved or have improved significantly. Still, the blue and red  $G_{BP}$  and  $G_{RP}$  photometry has a series of issues of its own. This photometry is based on prism spectra and has therefore – by design – a limited angular resolution. Each observation contains a substantial flux from the sky background, limiting the performance for faint sources. To help judge the reliability of the photometry, the excess factor, `phot_bp_rp_excess_factor`, gives a simple measure of the consistency between the three fluxes. For  $G_{BP}$  and  $G_{RP}$ , which collect the flux in a relatively wide window, the number of transits with other sources within (`phot_bp_n_blended_transits`) or close to (`phot_bp_n_contaminated_transits`) the window, can be useful but it is important to only count, of course, well known sources.

For the photometry we notice the following.

- The trend in  $G$  as a function of  $G$ , which was pronounced in *Gaia* DR2, has been significantly reduced in *Gaia* EDR3.
- The indications of a discontinuity in the  $G$  magnitude around  $G = 10.87$  and 13 mag are much weaker in *Gaia* EDR3 than in *Gaia* DR2, cf. Sect. 4.4.1.
- Sources, where a reliable colour was not known at the beginning of the *Gaia* EDR3 processing were processed using a default colour. They constitute a significant fraction of the catalogue and Riello et al. (2020) recommend a correction to the  $G$  photometry for such sources, in particular those with astrometric 6p solutions, see Sect. 4.3 for example, where it

<sup>15</sup> [https://gea.esac.esa.int/archive/documentation/GEDR3/Gaia\\_archive/chap\\_datamodel/](https://gea.esac.esa.int/archive/documentation/GEDR3/Gaia_archive/chap_datamodel/)



is demonstrated to work. The correction is typically a hundredth of a magnitude and can of course only be applied if a reliable colour is now known, which is the case for 86% of the 6p solutions.

- The  $G_{BP}$  and  $G_{RP}$  photometry is much less affected by systematic errors in the background subtraction than they were in *Gaia* DR2.
- The completeness of  $G_{BP}$  and  $G_{RP}$  is reduced in dense fields.
- Photometry in  $G_{BP}$  that is fainter than about 20.5 mag and in  $G_{RP}$  that is fainter than about 20 mag is heavily biased towards brighter values as illustrated in the simulations in Figs. 29 and 30. The cause is discussed in Riello et al. (2020) and well understood, cf. Sect. 4.2. We therefore recommend the use of the colour  $G - G_{RP}$  instead of  $G_{BP} - G_{RP}$  for samples including faint, red sources ( $G_{BP}$  fainter than about 20.5 mag).

Also a global, statistical analysis, cf. Sect. 5, confirms that the systematics of *Gaia* EDR3 have improved significantly compared to that of *Gaia* DR2. The more notable improvement, seen in this way, is found for the photometry, since some ‘systematics’ associated to the imprint of the scanning law pattern are still present in the astrometric parameters and their uncertainties.

*Acknowledgements.* This work has made use of data from the European Space Agency (ESA) mission *Gaia* (<https://www.cosmos.esa.int/gaia>), processed by the *Gaia* Data Processing and Analysis Consortium (DPAC, <https://www.cosmos.esa.int/web/gaia/dpac/consortium>). Funding for the DPAC has been provided by national institutions, in particular the institutions participating in the *Gaia* Multilateral Agreement. This work was supported by the Spanish Ministry of Science, Innovation and University (MICIU/FEDER, UE) through grants RTI2018-095076-B-C21, ESP2016-80079-C2-1-R, and the Institute of Cosmos Sciences University of Barcelona (ICCUB, Unidad de Excelencia ‘María de Maeztu’) through grants MDM-2014-0369 and CEX2019-000918-M. TM, DB, AG and EL acknowledge financial support from the Agenzia Spaziale Italiana (ASI) provided through contracts 2014-025-R.0, 2014-025-R.1.2015 and 2018-24-HH.0 to the Italian Istituto Nazionale di Astrofisica. PK acknowledges support from the European Research Council (ERC) under the European Union’s Horizon 2020 research and innovation programme under grant agreement No 695099 (project CepBin), and the French Agence Nationale de la Recherche (ANR), under grant ANR-15-CE31-0012-01 (UnlockCepheids). This research has made an extensive use of Aladin and the SIMBAD, VizieR databases operated at the Centre de Données Astronomiques (Strasbourg) in France and of the software TOPCAT (Taylor 2005). We finally wish to thank Alessandro Spagna for his comments to an earlier version of this paper.

## References

- Ahumada, R., Allende Prieto, C., Almeida, A., et al. 2020, *ApJS*, 249, 3
- Arenou, F., Lindegren, L., Froeschle, M., et al. 1995, *A&A*, 304, 52
- Arenou, F., Luri, X., Babusiaux, C., et al. 2018, *A&A*, 616, A17
- Arenou, F., Luri, X., Babusiaux, C., et al. 2017, *A&A*, 599, A50
- Bedin, L. R., Anderson, J., Heggie, D. C., et al. 2013, *Astronomische Nachrichten*, 334, 1062
- Betoule, M., Mignard, J., Bratslavsky, N., et al. 2013, *A&A*, 552, A124
- Bohlin, R. C., Gordon, K. D., & Tremblay, P. E. 2014, *PASP*, 126, 711
- Bovy, J., Nidever, D. L., Rix, H.-W., et al. 2014, *ApJ*, 790, 127
- Brandt, T. D. 2018, *ApJS*, 239, 31
- Cantat-Gaudin, T., Anders, F., Castro-Ginard, A., et al. 2020, *A&A*, 640, A1
- Chambers, K. C., Magnier, E. A., Metcalfe, N., et al. 2016, *ArXiv e-prints* [[arXiv:1612.05560](https://arxiv.org/abs/1612.05560)]
- Charlot, P., Jacobs, C. S., Gordon, D., Lambert, S., & et al. 2020, *A&A*, in press
- Clem, J. L. & Landolt, A. U. 2013, *AJ*, 146, 88
- Clem, J. L. & Landolt, A. U. 2016, *AJ*, 152, 91
- Clementini, G., Ripepi, V., Molinaro, R., et al. 2019, *A&A*, 622, A60
- de Bruijne, J. H. J., Allen, M., Azas, S., et al. 2015, *A&A*, 576, A74
- Dias, W. S., Monteiro, H., Caetano, T. C., et al. 2014, *A&A*, 564, A79 (DAML Catalogue)
- Gaia* Collaboration, Brown, A., Vallenari, A., & et al. 2020, *A&A* in press
- Gaia* Collaboration, Brown, A. G. A., Vallenari, A., et al. 2018, *A&A*, 616, A1
- Gaia* Collaboration, Prusti, T., de Bruijne, J. H. J., et al. 2016, *A&A*, 595, A1
- Górski, K. M., Hivon, E., Banday, A. J., et al. 2005, *ApJ*, 622, 759
- Kervella, P., Gallette, A., Evans, N. R., et al. 2019, *A&A*, 623, A117

- Kharchenko, N. V., Piskunov, A. E., Schilbach, E., Röser, S., & Scholz, R.-D. 2013, *A&A*, 558, A53 (MWSC Catalogue)
- Klioner et al. 2020, *A&A* in prep.
- Lallement, R., Babusiaux, C., Vergely, J. L., et al. 2019, *A&A*, 625, A135
- Landolt, A. U. 1983, *AJ*, 88, 439
- Landolt, A. U. 1992, *AJ*, 104, 340
- Landolt, A. U. 2007, *AJ*, 133, 2502
- Landolt, A. U. 2009, *AJ*, 137, 4186
- Landolt, A. U. 2013, *AJ*, 146, 131
- Lejeune, T., Cuisinier, F., & Buser, R. 1997, *A&AS*, 125, 229
- Lindegren, L., Bastian, U., Biermann, M., et al. 2020a, *A&A* in prep.
- Lindegren, L., Hernández, J., Bombrun, A., et al. 2018a, *Gaia* DR2 astrometry, IAU 30 GA – Division A: Fundamental Astronomy, Vienna, 2018 August 2
- Lindegren, L., Hernández, J., Bombrun, A., et al. 2018b, *A&A*, 616, A2
- Lindegren, L., Klioner, S., Hernández, J., et al. 2020b, *A&A* in prep.
- Mason, B. D., Wycoff, G. L., Hartkopf, W. I., Douglass, G. G., & Worley, C. E. 2001, *AJ*, 122, 3466
- Nascimbeni, V., Bedin, L. R., Heggie, D. C., et al. 2014, *MNRAS*, 442, 2381
- Riello, M., De Angeli, F., Evans, D. W., et al. 2020, submitted to *A&A*
- Rowell, N., Davidson, M., Lindegren, L., et al. 2020, submitted to *A&A*
- Sarajedini, A., Bedin, L. R., Chaboyer, B., et al. 2007, *AJ*, 133, 1658
- Seabroke, G., Fabricius, C., Teyssier, D., et al. 2020, submitted to *A&A*
- Taylor, M. B. 2005, in *Astronomical Society of the Pacific Conference Series*, Vol. 347, *Astronomical Data Analysis Software and Systems XIV*, ed. P. Shopbell, M. Britton, & R. Ebert, 29
- Torra, F., Castañeda, J., Fabricius, C., et al. 2020, submitted to *A&A*
- Udalski, A., Szymanski, M. K., Soszynski, I., & Poleski, R. 2008, *Acta Astron.*, 58, 69

## **Appendix A: Completeness in globular clusters**

## **Appendix B: *Gaia*-specific terms**

Below, in Table B.1, we give short definitions of *Gaia*-related terms appearing in this paper. Several are fields in the *Gaia* catalogue and detailed explanations are available in the *Gaia* EDR3 datamodel description.

**Table A.1.** Completeness tables for 26 GCs. Core:  $r < 0.5$  arcmin. Out:  $0.5 < r < 2.2$  arcmin.

Name	Region	$G$									
		11 – 13	12 – 14	13 – 15	14 – 16	15 – 17	16 – 18	17 – 19	18 – 20	19 – 21	20 – 22
LYN07	core	–	–	–	–	–	–	50	37	14	4
LYN07	out	–	–	–	–	57	52	39	34	19	6
NGC0104	core	40	7	2	0	0	0	0	0	0	0
NGC0104	out	100	75	68	47	22	3	1	0	0	0
NGC0288	core	–	–	–	–	–	–	72	51	21	3
NGC0288	out	–	–	–	99	92	89	81	67	37	10
NGC1261	core	–	–	–	82	77	57	20	2	0	0
NGC1261	out	–	–	–	100	100	94	73	42	18	4
NGC1851	core	–	–	50	42	31	13	2	0	0	0
NGC1851	out	–	–	–	99	94	80	50	25	10	2
NGC2298	core	–	–	–	–	89	85	52	23	8	2
NGC2298	out	–	–	–	–	98	96	92	83	58	19
NGC4147	core	–	–	–	–	–	73	50	24	9	2
NGC4147	out	–	–	–	–	–	100	87	85	44	12
NGC5053	core	–	–	–	–	–	–	–	96	61	20
NGC5053	out	–	–	–	–	–	100	96	97	65	19
NGC5139	core	–	–	25	19	6	0	0	0	0	0
NGC5139	out	97	64	51	38	13	1	0	0	0	0
NGC5272	core	–	–	74	62	45	12	1	0	0	0
NGC5272	out	–	100	100	93	84	56	25	9	2	0
NGC5286	core	–	–	68	55	39	19	3	0	0	0
NGC5286	out	–	–	91	94	89	74	50	21	6	1
NGC5466	core	–	–	–	–	–	–	–	79	46	14
NGC5466	out	–	–	–	–	100	100	98	97	67	21
NGC5927	core	–	–	–	79	77	61	16	1	0	0
NGC5927	out	–	–	91	83	87	80	58	19	5	0
NGC5986	core	–	–	–	66	64	41	10	0	0	0
NGC5986	out	–	–	93	90	92	79	54	22	7	1
NGC6121	core	–	–	–	76	64	47	23	3	0	0
NGC6121	out	–	96	93	86	85	74	58	36	12	1
NGC6205	core	–	–	89	65	35	7	0	0	0	0
NGC6205	out	98	100	100	95	81	47	16	4	0	0
NGC6366	core	–	–	–	–	–	–	78	69	52	20
NGC6366	out	–	–	–	89	85	82	85	82	62	24
NGC6397	core	–	–	68	55	41	21	6	0	0	0
NGC6397	out	–	100	98	90	84	73	53	30	9	1
NGC6656	core	–	–	82	63	24	3	0	0	0	0
NGC6656	out	94	93	85	75	55	17	3	0	0	0
NGC6752	core	–	85	61	39	14	3	0	0	0	0
NGC6752	out	–	100	100	93	78	48	22	6	0	0
NGC6779	core	–	–	–	–	83	72	37	7	1	0
NGC6779	out	–	–	92	90	88	86	72	51	24	5
NGC6809	core	–	–	–	–	–	59	29	6	0	0
NGC6809	out	–	–	100	100	93	81	53	19	2	0
NGC6838	core	–	–	–	–	–	79	68	44	15	1
NGC6838	out	–	–	93	91	78	87	84	70	41	9
NGC7099	core	–	–	–	56	41	17	5	1	0	0
NGC7099	out	–	–	–	100	91	77	56	34	13	2
PAL01	core	–	–	–	–	–	–	–	–	86	47
PAL01	out	–	–	–	–	–	–	–	84	80	28
PAL02	core	–	–	–	–	–	–	93	80	37	12
PAL02	out	–	–	–	–	–	–	92	91	62	22

**Table B.1.** Short definitions for *Gaia*-related terms.

Term	Description
AC	<i>Gaia</i> ACross scan (direction)
astrometric_gof_al	GoF for the astrometric solution
GoF	goodness of fit, reduced $\chi^2$ , e.g. for image fitting or for the astrometric solution
IPD	Image Parameters Determination, estimating location and flux for each CCD window
ipd_frac_multi_peak	percentage of CCD transits where additional images were seen
ipf_frac_odd_win	percentage of incompletely sampled CCD transits
ipd_harmonic_gof_amplitude	scan angle dependent variation of GOF for the image fitting
ipd_harmonic_gof_phase	phase of the IPD GoF versus position angle of scan
parallax_over_error	$\varpi/\sigma_\varpi$
PhotPipe	photometric pipeline, software system for the photometric calibration
phot_bp_rp_excess_factor	sum of $G_{BP}$ and $G_{RP}$ fluxes divided by the $G$ flux
pseudocolour	wave number determined as the 6th parameter for 6p astrometric solutions
ruwe	renormalised unit weight error
SSC	spectral shape coefficient: the flux in a certain section of the $G_{BP}$ or $G_{RP}$ spectrum
visibility period	set of transits for a source with no time gap exceeding four days